Bruno Miguel Gomes Conceição

An Electrical Current Sensor for Aerospace Applications

Dissertation presented to the Physics Department at
University of Coimbra to obtain the Master's degree in Physics Engineering

15 of September of 2017

UNIVERSIDADE DE COIMBRA

University of Coimbra

Master's Thesis

An Eletrical Current Sensor for Aerospace Applications

Bruno Miguel Gomes Conceição

*A thesis submitted in fulfillment of the requirements
for the Master's Degree in Physics Engineering*

Supervisors:
Prof. Dr. Francisco Cardoso
Eng. Bruno Antunes

September 15, 2017

Abstract

The development of an electrical current sensor applied to the aerospace sector is presented. The sensor has a closed loop topology and AMR technology is used as an transducer element, options that were defined through a comparative study and simulation of magnetic fields generated by the passage of electrical currents that will be measured. The simulations were performed using a commercial Finite Element Method (FEM) program. The sensor was designed, manufactured and demonstrated, obtaining perfectly satisfactory results in face of the requirements.

Resumo

O desenvolvimento de um sensor de correntes elétricas com aplicação para o sector aeroespacial é aqui apresentado. O sensor tem uma topologia de realimentação fechada e utiliza a tecnologia AMR como elemento transdutor, opções feitas através de um estudo comparativo e simulação de campos magnéticos gerados pela a passagem de correntes elétricas a medir. As simulações foram realizadas com um software comercial de elementos finitos. O sensor foi projetado, realizado e demonstrado tendo-se apresentado os resultados perfeitamente satisfatórios face aos requisitos.

Dedicado ao Beto. . .

Contents

List of Figures

List of Tables

List of Abbreviations

AC	Alternating Current
AMR	Anisotropic Magnetoresistance
COTS	Commercial of the Shelf
DC	Direct Current
ECSS	European Cooperation for Space Standardization
EMI	Electromagnetic interference
ESA	European Space Agency
FFT	Fast Fourier Transform
IC	Integrated Circuit
LHCP	Left-Hand Circular Polarized
MR	Magnetoresistance
PCB	Printed Circuit Board
PDCU	Power Conditioning and Distribution Unit
TLR	Technology Readiness Level
PCB	Printed Circuit Board
RHCP	Right-Hand Circular Polarized

List of Symbols

μ	Magnetic Permeability.
ρ	Density.
σ	Electric Conductivity.
A	Magnetic Potential
B	Magnetic Flux Density.
E	Electric Field Strength.
I	Electric Current
J	Current Density.
R	Resistance.
T	Temperature.
V	Voltage.
v	Velocity vector.

Chapter 1

Introduction

1.1 Motivation

One of the most adopted power harvesting techniques in space applications is based on solar energy, which is converted to electric energy by means of solar arrays. Due to the intrinsic characteristics of such energy source, together with the typical requirements applicable to spacecraft and space systems in general, a Power Conditioning and Distribution Unit (PCDU) for a space application is a highly critical subsystem, with tough complexity and requirements. The electrical efficiency of a PCDU is typically one of the most challenging requirements. Amongst many other factors, the need for electric current measurement in several locations of the electrical energy flow path within the PCDU domain may have a huge impact on the device performance. Furthermore, the need for current measurement within a space system is not limited to the PCDU domain. Each instrument or device integrated to the system needs to use electric current measurement at some stage of its power management functions. Commercial of the Shelf (COTS) components dedicated to current measurement in an aerospace application are not available or are very difficult to find, leading the need for its use to develop custom design within each application. The design of a solution aiming at measuring electric current in a space environment, which is applicable to a wide range of aerospace applications requirements would be beneficial for higher level system design, due to the shortening of development time, cost and risk, amongst other factors.

1.2 Objectives

The work presented and discussed in this thesis is the development of a high efficiency electric current measurement device focused on the aerospace needs and European Cooperation for Space Standardization (ECSS) standards.

1.3   Dissertation overview

The structure of this Dissertation is as follows:

In Chapter 2, the objective is to give an overview of what are the boundary conditions and the validating technology issues of a space instrument development.

In Chapter 3, a comparison analyses between several current measurement techniques is done. It is then chosen the right technology, for the problem to solve, with the aid of numerical simulations.

Chapter 4 presents the sensor design, each subsystem is explained and it ends with the simulation of each one in a SPICE model.

In Chapter 5, the sensor is tested in real world conditions and the results are discussed.

Finally, in Chapter 6, conclusions are drawn and further work is proposed.

Chapter 2

Instrumentation in Space

The interplanetary space frequently means having extreme conditions, such as extreme heat and cold cycling, ultra-vacuum and high energy radiation. These extreme conditions are threats to many materials and components of spacecrafts and satellites, leading to a faster degradation and failure. For a space instrumentation project, it is fundamental to present various issues that affect electronic circuits in space environment, and their consequences. Hence, this chapter provides a brief introduction to space environment and its impact in space instrumentation and which standards are used in the space industry and how the maturity of a space technology is estimated.

2.1 Environmental boundary conditions

2.1.1 Vaccum

The hard vacuum of space (10^{-6} to 10^{-9} torr) will cause outgassing, which is the release of volatiles from materials [1]. This molecular contamination can affect optical properties of vehicle and payload surfaces as well as spacecraft performance. Having no atmosphere in space also poses a problem for heat sink, since cooling in the form of convection cannot take effect.

2.1.2 Temperature

As satellites and spacecraft move in and out of the sunlight during its orbit around Earth, they experience extreme thermal cycling temperatures. A rule of thumb for these cyclic temperature variations is that they vary between $-120\,°C$ to $120\,°C$. A few thermal cycles can lead to cracking, peeling, spalling or formation of pinholes in some materials. These temperature variations are also important in electronic components, as some of them experience thermal drift, inducing malfunctions.
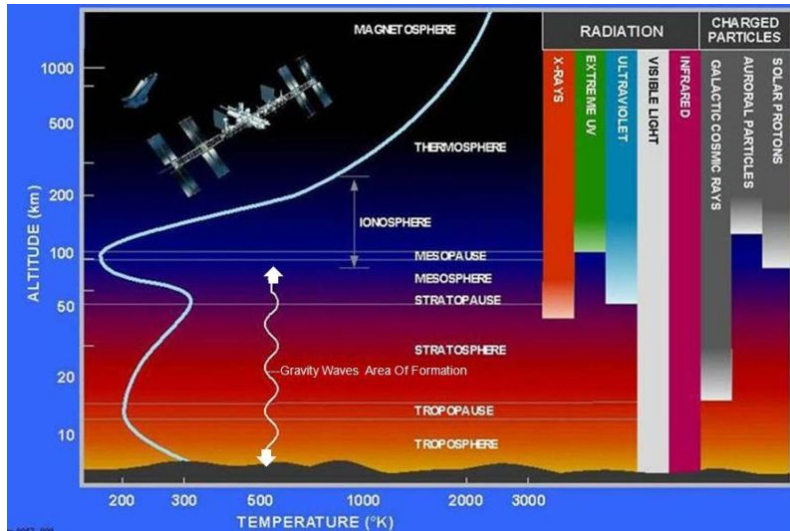
FIGURE 2.1: Temperature range and radiation in the Earth's atmosphere [2].

2.1.3   Electromagnetic Interference

Electromagnetic interference (EMI) can cause signal degradation and may therefore induce errors in control circuits due to the appearance of excessive unwanted noise. Radio frequency telecommunications can also be accounted for magnetic interference in free space [3].

In order to mitigate EMI problems, input filters can be added and, also , special attention as to be praid to Printed Circuit Board (PCB) design such as trying to use the shortest possible strip lines and also ensure small loops. These measures reduce parasitic inductances that are responsible for crosstalk.

2.1.4   Radiation

The three main sources of charged particle radiation naturally occurring in space are galactic cosmic rays, solar proton events, and the trapped radiation belts.

Radiation with enough energy to penetrate the shielding of a satellite or spacecraft can cause ionization events in critical electronics and consequently, spacecraft charging, which can cause sudden failure of a system at any point in its mission. The damage effects caused by high-energy radiation can reduce mission lifetimes due to long-term damage to devices, integrated circuits (ICs), or solar cells [4]. Radiation effects can be alleviated by using additional shielding, error-correction circuitry, and triple-module redundancy, where two good process results outvote a corrupted one.[1]

2.2 Validating technology: fundamental issues

2.2.1 Technology Readiness Level

Technology Readiness Level (TRL) is a method of estimating technology maturity of a particular technology. Each project is evaluated against the parameters for each technology level and is then assigned a TRL rating based on the project's progress. TRL is usually split in nine levels, where TRL 1 is the lowest and TRL 9 is the highest. The use of TRL enables consistent, uniform discussions of technical maturity across different types of technology. Different definitions are used but as the project was developed in Europe, the European definition will be employed (Table 2.1). Although they are conceptually similar, significant differences exist in terms of maturity at a given technology readiness level. European Space Agency (ESA) is using the ISO standard 16290 Space systems Definition of the Technology Readiness Levels and their criteria assessment.

TABLE 2.1: Technology Readiness Level Summary

TRL	Level Description
1	Basic principles observed and reported
2	Technology concept and/or application formulated
3	Analytical and experimental critical function and/or characteristic proof-of-concept
4	Component and/or breadboard functional verification in laboratory environment
5	Component and/or breadboard critical function verification in relevant environment
6	Model demonstrating the critical functions of the element in a relevant environment
7	Model demonstrating the element performance for the operational environment
8	Actual system completed and accepted for flight ("flight qualified")
9	Actual system "flight proven" through successful mission operations

A good example of the use of TRL is in the qualification of an electronic component. After the first levels of functional verification and testing the sensor in a simulated space environment, the electronic component is only space qualified when a successful system flight is made.

2.2.2 European Cooperation for Space Standardization

The European Cooperation for Space Standardization (ECSS), established in 1993, is an organization that works to improve standardization within the European space sector. The ECSS frequently publishes standards, to which contractors working for ESA must adhere to. The goal of this standardization system is to minimise life-cycle cost, while improving the quality, functional integrity, and compatibility of all elements of a space project. This goal is achieved by applying common standards not only for development of hardware and software but also for project management.

2.3   Project Guidelines

The level of maturation of the project in which this thesis is aggregated to is in a TRL 3 level, on its way to TRL 4. This means that a proof-of-concept was previously made and now a breadboard functional verification in a laboratory environment is being developed. Beside the standards of project management being applied by Active Space Technologies, one of the standards applied was the *ECSS-Q-ST-70-12C*, which is a Standard for PCB Design, presenting constraints and guidelines to the development of the PCB, as shown in Chapter 3. In this design, all electronic components were a commercial equivalent of a space qualified component, which implies that when the project advances to TRL 5, all electronic components are ready for space conditions.

Chapter 3

Transducer Selection

The transducer is a crucial element, being the heart of the sensor, it is sensitive to the variable needed to measure. Therefore, the transducer selection strategy begins by studying the current state of technology in current measurement, then choosing the applicable technology in accordance with the project requirements and with the results of numerical simulations.

3.1   Current Measurement: techniques and transducers

This section will present the current state of technology to be employed in this dissertation.

3.1.1   Non-Isolated Current Measurement Techniques

Non-isolated techniques are based on the Ohm's law of resistance.

Shunt Resistor

A common approach due to its simplicity is the use of a shunt resistor for current sensing. The voltage drop across the shunt resistor is used as a proportional measure of the current flow. Using shunt resistors for current sensing are the most cost effective sensing elements, having compact package profiles and being suitable for Direct Current(DC) or Alternating Current (AC) measurement. Although current shunts operate on the principle of the Ohmic voltage drop, practical shunts have intrinsic inductance, which limits the accuracy and bandwidth [5].
When using shunt resistors, there is no galvanic isolation between the input current and the sensing circuit and can, therefore, generate a substantial amount of power loss. The power loss can be calculated via Ohm's Law leading to:

$$P = I^2 R. \tag{3.1}$$

This power loss can be a serious handicap for high current applications.

3.1.2 Isolated Current Measurement Techniques

When galvanic isolation between the current to be measured and the sensor is required, the measurement principle is based on effects caused by the magnetic field of the current. These effects are Ampère's Circuital Law, Faraday's Law of Induction, and the Faraday Effect. Ampère's Circuital Law and the Faraday's Law of Induction are used in several traducers, sometimes at the same time. On the other hand the Faraday Effect is only used in magneto-optical sensors, so this effect will only be explained in the magneto-optical sensor section.

Alongside those fundamental physical principles, it is equally important to take into account the three existing sensing topologies. These are Open-Loop, Closed-Loop and a third method which combines multiple techniques, for example a magnetic sensor with a current transformer.

Rogowzski Coil

The Rogowzski Coil consists of an air-cored coil placed around the conductor in a toroidal fashion as shown in Figure 3.1. By Ampere's Law, the current in the conductor will create a magnetic field. The rate of change of current in the conductor will induce a voltage in the coil as explained by Faraday's law. Therefore, the output of the Rogowski coil is usually connected to an integrator circuit to provide an output signal that is proportional to the current.

FIGURE 3.1: Basic configuration of a Rogowski Coil [5].
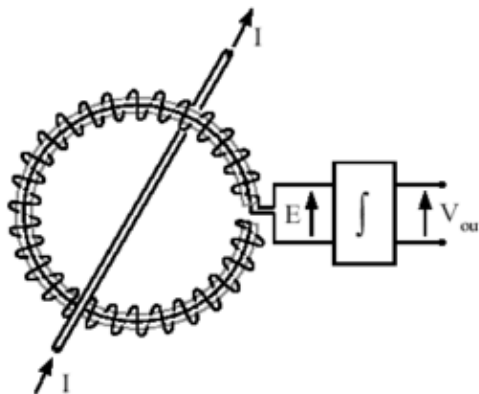
Since practical integrators are not perfect and may exhibit a small but steady input offset voltage, its frequency response must be altered, so that the gain at low frequency is reduced. Hence, practical Rogowski coils are not suitable to measure low-frequency currents [6]. The Rogowski coils thermal drift is determined, not only by the integrator but also due to the

fact that the thermal expansion of the coil the cross-sectional area A of the coil body may change.

This type of transducers has the following features [5]:

- High Bandwidth;

- Capability of measuring large currents (The same size coil can be used for measuring 100A or 100 kA);

- Non-saturation because of air core;

- Isolation and non-intrusive measurement between testing circuit and transducer;

- Good linearity due to absence of magnetic material;

- Compact and light weight;

Current Transformer

Current transformers (CT) have been widely used for AC current sensing with its bandwidth up to tens of MHz. Similar to the Rogowski coil, the CT also exploits Faradays law of induction to measure currents. The construction is basically the same as the Rogowski coil, with one single primary turn and multiple secondary turns, but it also employs a core material with high relative permeability. The main difference between a CT and a Rogowski coil is that the secondary winding of the current transformer is loaded with a sense resistor R_s.
Having an output voltage directly proportional to the primary current is an advantage of a current transformer over the Rogowski coil, since no integrator is required that may deteriorate the accuracy by its offset drift or output saturation.

Magneto-optical sensor

One of Faradays many discoveries was that circular birefringence can be induced into a material by applying a magnetic field parallel to the light propagation direction. If the intrinsic circular birefringence of a medium is negligibly small, the rotation plane of the polarization of linear polarized light is proportional to the integral of applied magnetic field H along the path s:

$$\theta = V \int \boldsymbol{H} \cdot \boldsymbol{ds}, \tag{3.2}$$

where the constant of proportionality V is the Verdet constant, a property of the medium through which light travels that describes the strength of the Faraday Effect. See Figure 3.2.

Linear polarized light can be thought of as being composed of two orthogonal circular polarized light waves. In particular, a linear polarized light wave is the superposition of a right-hand circular polarized (RHCP) light wave orthogonal to a left-hand circular

polarized (LHCP) light wave. In the Faraday effect, the velocity of the RHCP light waves is decreased if the magnetic field is pointing along its propagation direction, and increased when the magnetic field points in the opposite direction. LHCP light waves behave vice-versa. This means that if linearly polarized light, which is the superposition of RHCP and LHCP light, is fed into a material undergoing the Faraday effect there will be a phase difference induced between the two different circularly polarized beams and as, a result the polarization plane of the linear polarized light is rotated. Knowing how much it rotated allows to know the magnetic field intensity and thus the electrical current. To use this effects, it is required a complex setup that consumes a lot of space and energy. Due to high complexity, this effect it not suitable to measure small currents [6].
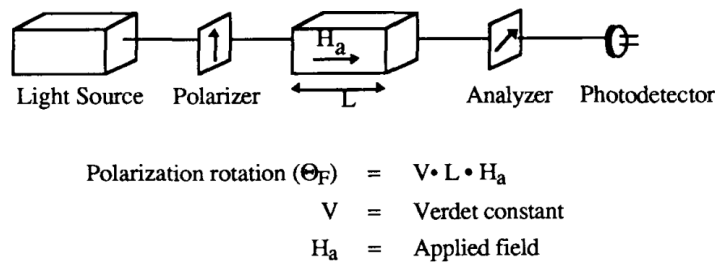
FIGURE 3.2: Simplified scheme of a Magneto-Optical Sensor [7].

Magnetic Sensors

Figure 3.3 presents a sketch describing the most significant applications as a function of magnetic sensor type and dynamic range, from 1 fT to 10 kT. Magnetic sensors include scalar and vector magnetometers. For this application we want technologies with a large dynamic range around 10^{-4} T, which include Hall effect, fluxgate, search coil and a variety of magnetoresistance effects.
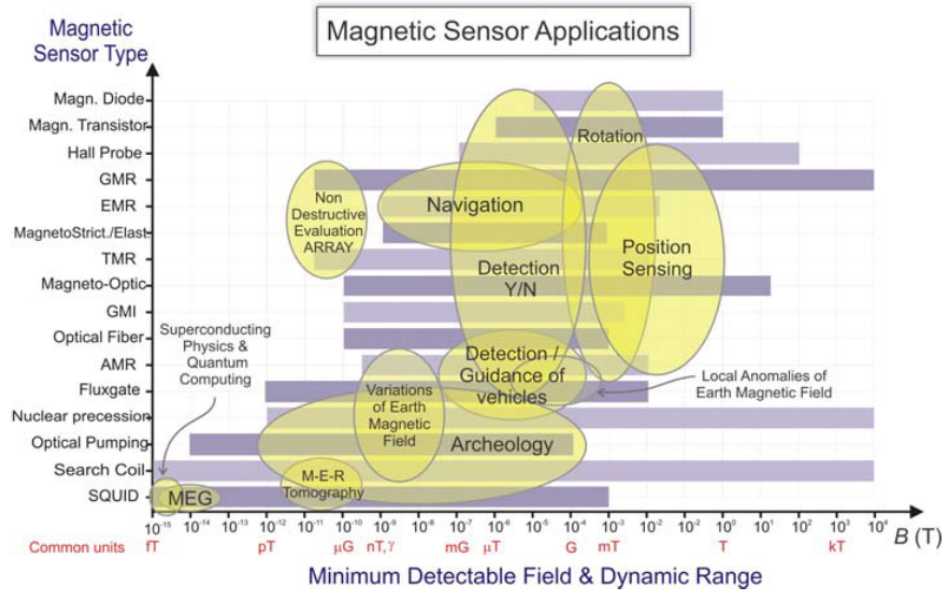
FIGURE 3.3: Magnetic Sensors Technologies: Magnetic properties (dynamic ranges and minimum detectable field) and applications [8].

Hall Effect

One of the most popular magnetic sensors is the Hall Effect sensor. The sensor, illustrated in Figure 3.4, is based on the Hall effect, which was discovered by Edwin Hall in 1879. He found that a voltage difference V, appears across a thin rectangle of gold placed in a strong magnetic field B, perpendicular to the plane of the rectangle when an electric current I, is set along its length. An electron moving through a magnetic field experiences a force, the Lorentz force, that is perpendicular both to its direction of motion and to the direction of the field. This force is responsible for the Hall voltage, given by:

$$V = \frac{IB}{nqd},$$ (3.3)

where q is the charge of the current carrier, n the carrier density and d the thickness of the sheet.
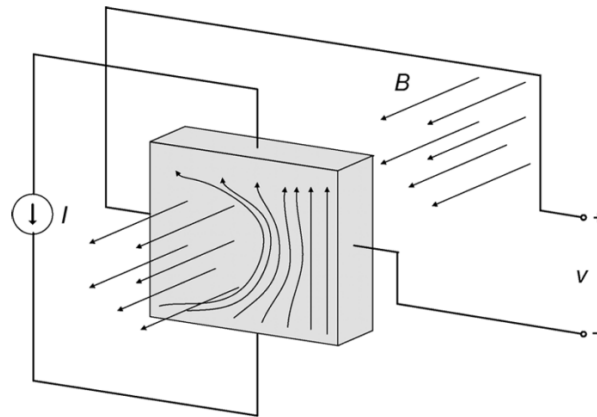
FIGURE 3.4: Due to the Lorentz law, a flowing current I through a thin sheet of conductive material experiences a force if an external magnetic field B is applied. Therefore, at one edge of the sheet the density of conductive carrier is higher, resulting in a voltage potential V that is proportional to the magnetic field B [6].

The Hall effect is very small in metallic conductors, but a semiconductor gives a much larger effect. Since there are fewer conduction electrons in a semiconductor, if the total current through it is the same as that through a metal, the electrons in the semiconductor must have a greater drift velocity than those in the metal. The faster the electrons are moving, the stronger the force they experience and the greater the Hall voltage produced at equilibrium. The equation is valid for materials in which the electrical conductivity is mediated by either positive or negative charge carriers. This is the case for conductors, while for semiconductors a more complex coherence exists.

$$R_H = \frac{1}{nq}. \tag{3.4}$$

With no magnetic field present, an offset voltage is present at the output, also known as misalignment voltage. Thus, to use the Hall effect as a current sensor, additional circuitry is required, particularly to compensate for the misalignment voltage and the distinct thermal drift. Hall effect sensors are found in open-loop, closed-loop, and combined principles like ETA [9].

Fluxgate

The fluxgate technology is known for decades and is one of the most accurate magnetic field sensors available today with patents dating back 1931 [7]. The basic fluxgate principle exploits the non-linear relation that exists between the magnetic field H, and the magnetic flux density B, within a magnetic material. These sensors are able to measure DC or low-frequency AC magnetic fields.

The most common type of fluxgate is called the second harmonic device presented in Figure 3.5. It exploits the magnetic induction together with the hysteresis exhibited by all ferromagnetic materials. Hysteresis is the dependence of the state of a physical system

on its previous history. In this case, the term refers to the fact that the magnetic flux through the ferromagnetic core lags behind changes in the magnetic field.

When a sinusoidal current is applied to one of the coils, the current magnetizes the core, causing it to reach its saturation magnetization once each half-cycle. Because of hysteresis, the magnetic flux through the core will trace a loop if it is plotted against the magnetic field intensity, as shown in figure 3.5. Changes in flux density through the core are sensed by the second coil. As the core is driven into saturation, the reluctance of the core to the external magnetic field being measured increases, thus making it less attractive for the magnetic field to pass through the core. As this field is repelled, its change is sensed by the second coil. When the core comes out of saturation by reducing the current in the drive coil, the external magnetic field is again attracted to the core, which is again sensed by the second coil. The voltage output from the second coil consists of even-numbered harmonics of the excitation frequency. For readout, the second harmonic is extracted and rectified. The voltage associated with this harmonic is proportional to the external magnetic field.

Another way of looking at the fluxgate operating principle is to sense the resistance of saturating the core caused by a change in its magnetic flux. This difference is due to the external magnetic field.
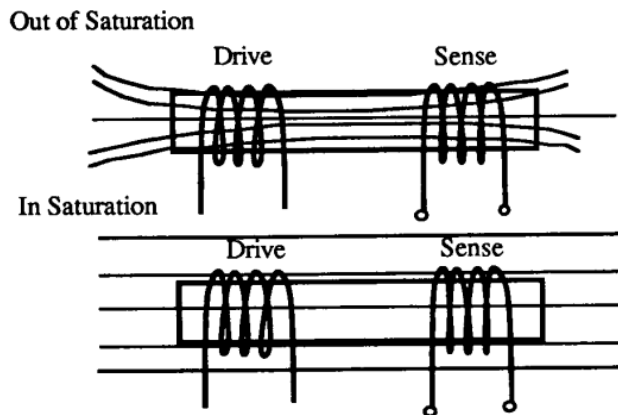

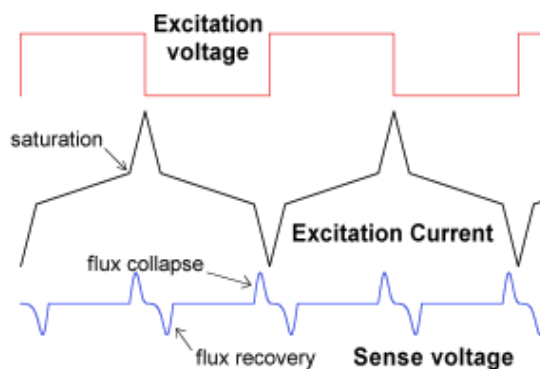FIGURE 3.5: Simplified scheme fluxgate principle[7].

FIGURE 3.6: Simplified waveforms in the fluxgate principle.

Many different fluxgate-based sensors have been proposed and there are efforts in integrating open-loop fluxgate sensors with PCB technology which is certainly a promising development towards low-cost applications. Standalone fluxgate sensors are commercially successful but so far only in high precision applications because of the high cost and size requirements.

Anisotropic Magnetoresistance (AMR)

William Thompson, later Lord Kelvin, first observed the magnetoresistance effect in ferromagnetic metals in 1856. The effect is known for a change in resistance caused by a external magnetic field. It is termed anisotropic because, in contrast to the previously known ordinary magnetoresistance, it depends on the angle between the electric current and the magnetization direction. Materials such as Permalloy (an alloy of nickel and iron) can be given a preferred magnetic orientation such that a current, passing trough a ribbon of material magnetizes it in a direction parallel to the direction of the current. If a magnetic field is then applied perpendicular to the current, the direction of magnetization will rotate toward the direction of the magnetic field. The angle through it which rotates depends on the amplitude of the external magnetic field. The resistance of the permalloy element decreases as the direction of the magnetization rotates away from the direction in which the current flows because the conduction electrons moving in the direction of magnetization have a greater probability to be scattered. In general, the resistance is given as a function of the angle, Θ,between the magnetization and current:

$$R = R_0 + \Delta R \cos^2(\Theta) \tag{3.5}$$

The Figure (3.7) illustrates the magnetoresistance effect.
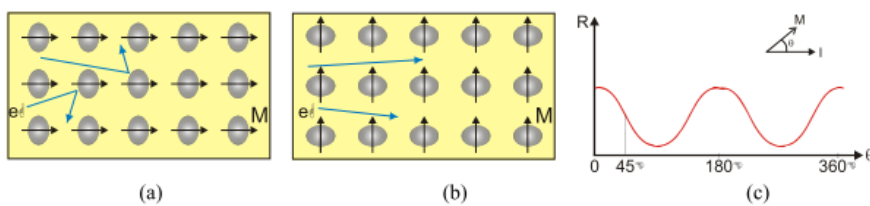
FIGURE 3.7: Illustration of AMR effect showing distortion of electron orbitals and resulting difference in scattering when the magnetization is (a) parallel to the current or (b) perpendicular to the current direction. (c) Variation of resistance as a function of angle between the current and magnetization. The optimum operating point is at $45°$[10]

This function, plotted in Figure 3.7c, shows that the maximum sensitivity and linearity is achieved when the magnetization is at $45°$ with respect to the current. The $45°$ alignment is commonly achieved by patterning diagonal stripes of highly conductive metal onto the more resistive Anisotropic Magnetoresistance (AMR) material as shown in Figure (3.8a). The current will then run perpendicular to these barber pole stripes while the magnetization vector remains preferentially along the long direction of the Magnetoresistance (MR)

device. The application of an external magnetic field will rotate the magnetization with a resulting change in resistance as shown in Figure 3.8b.

These kinds of sensors are very common in read heads for tape and disk drives. Other common applications include automotive wheel speed and crankshaft sensing, compass navigation, vehicle detection, current sensing and many others.
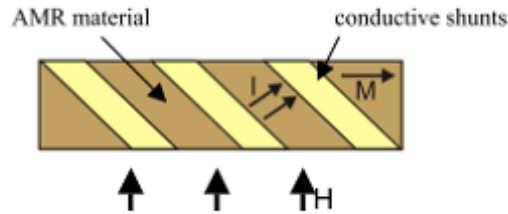
(A) Barber-pole structure of conductive shunts that constrain the current to run at 45° to the rest position for the magnetization.
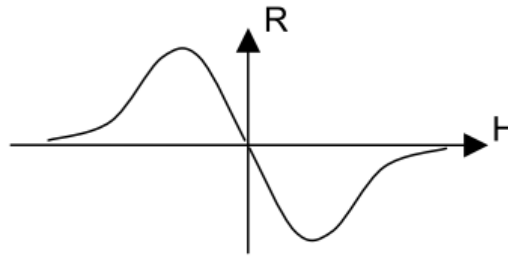
(B) Resistance versus field for a properly biased AMR device.

FIGURE 3.8: Barber Pole illustration [10]

.

Giant MagnetoResistance (GMR)

The giant magnetoresistance effect in thin-film multilayers was discovered in 1988 by Baibich and co-workers at the Université Paris-Sud [10]. The term giant magnetoresistance was coined because the 10 - 15 % change in resistance found in GMR far exceeds that of any AMR devices. The resistance of two ferromagnetic layers separated by a thin non-magnetic conducting layer can be altered by changing whether the moments of the ferromagnetic layers are parallel or anti-parallel. Layers with parallel magnetic moments will have less scattering at the interface, longer mean free paths, and lower resistance. Whereas layers with anti-parallel magnetic moments will have more scattering at the interfaces, shorter mean free paths, and higher resistance.
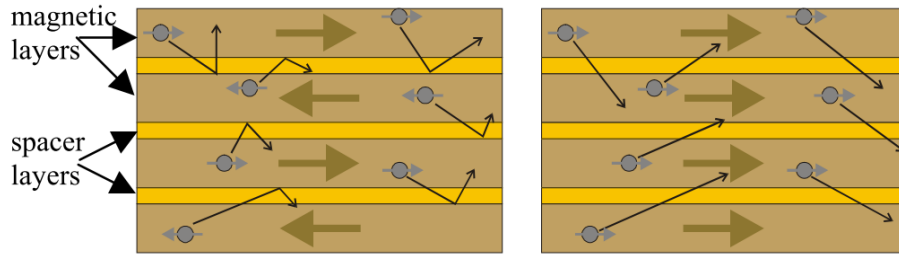
(A) Layers of alternating magnetization producing lots of scattering and re-duced scattering when the magnetization of the layers is aligned by an applied field.
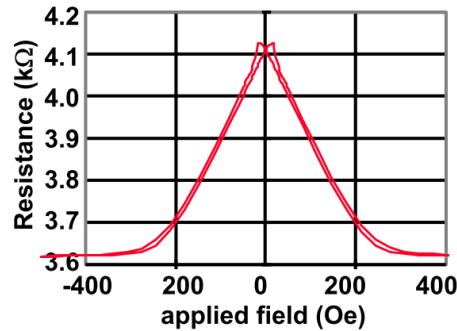
(B) Resulting variation in resistance as a function of applied field.

FIGURE 3.9: Illustration of the GMR effect[10].

General-purpose GMR commercial devices are fabricated by NVE Corp.

Future Magnetoresistance

Colossal Magnetoresistance, Tunneling Magnetoresistance and Giant Magneto Impedance are some of the technologies which are in its infancy and significant advances may be expected in the coming years. No commercial current sensors based on these effects are available but they have the potential to become more relevant in the future due to their very high sensitivity.

3.1.3   Sensing Topologies

Open-Loop

The open-loop configuration presents the simplest method to use a magnetic field sensor for current sensing. The Figure 3.10 describes its configuration. A magnetic field sensor is integrated in a SMD IC (integrated-circuit) and placed in close proximity to the current carrying conductor, i_c. The magnetic field around the copper trace carrying at a certain distance is proportional to the current at all times, as shown by Ampère's Circuital Law. The magnetic field sensor measures directly the magnetic field around the current carrying conductor.

This principle has the advantage of being simple and compact. The sensitivity, linearity and thermal drift are largely determined by the magnetic field sensor.
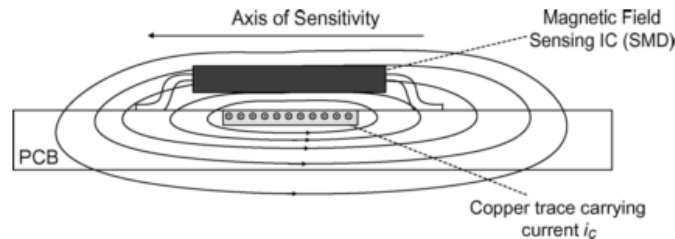

FIGURE 3.10: The simplest schematic for open-loop current measurement[6].

However, there are several disadvantages to the open-loop technique.

First, the bandwidth of the system is not only limited by the sensing element, but also by the required level of amplification of the output voltage. For high frequencies, if the sensor is located close to the current carrying conductor, the measurement accuracy may be further reduced by the skin effect, which forces high frequency current to flow along the outer edges of the conductor and thus changes the magnetic field at the sensor. The most serious disadvantage, however, is the susceptibility to stray external magnetic fields. These fields can significantly disturb the measurement accuracy. One of the solutions to this problem is to shield these fields. However, shielding is complicated because these shields employ materials with high conductivity and high permeability, shielding both static and dynamic fields. Moreover, the presence of a magnetic shield will also change the magnetic field at the sensors position, exhibit losses due to eddy currents, and change its permeability based on the offset magnetization and frequency. All this makes it very complicated to obtain a linear and reproducible relation between the current and measured magnetic field over a wide frequency range [6].

Closed-Loop

In a closed-loop configuration, the output voltage of the magnetic field sensor is used as an error signal to compensate the magnetization inside the magnetic core by forcing a current I_s through a second transformer winding [6]. This current generates a magnetic field that opposes the primary current I_c, as shown in Figure 3.11.

Assuming the current I_c perfectly compensates the magnetic flux, I_s is proportional to the primary current I_c. With this technique, there is no dependency with the magnetic sensor properties, greatly reducing the influence of thermal drift, and linearity also becomes independent of the magnetic field sensor. There will still be some offset voltage present due to the amplification stage and the remanence of the core material that may cause some temperature dependent drift. Excessive overcurrent can also change the offset voltage of this measurement principle and has to be removed by a degaussing cycle.
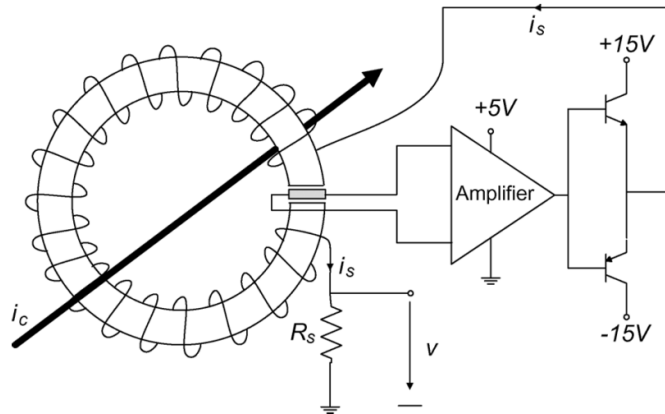
FIGURE 3.11: A closed-loop configuration in which a secondary winding is used to compensate the flux inside the transformer to zero, while the output voltage of the magnetic field sensor acts as an error signal. The current through the secondary winding can be measured to determine the magnitude of i_c[6].

Combination of Multiple Techniques

Sometimes it is useful to combine the properties of closed and open loop techniques. An example of this is the "Eta" current sensing principle developed by the company *LEM* [9]. They combined an open-loop magnetic field sensor, in this case a Hall effect device, using a magnetic core with the CT principle, as shown in Figure 3.12. Since no compensation current is required, the power consumption has been greatly reduced.

The current transformer covers the high-frequency range and the open-loop Hall effect element provides the low-frequency current information. In general the Eta technology-based current transducers are as expensive as closed loop Hall effect current transducers [6].
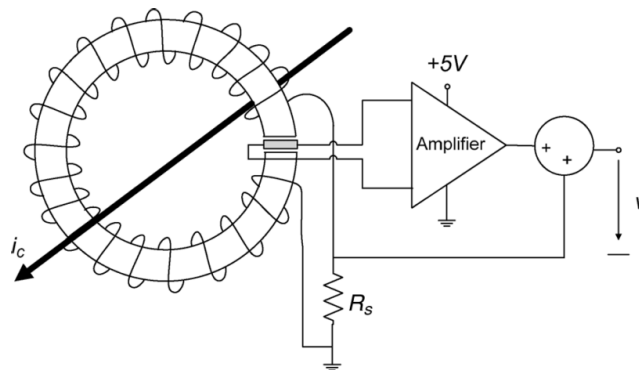
FIGURE 3.12: A schematic of the Eta technology, which combines the output of an open-loop Hall effect sensor and a current transformer to achieve a high band- width current transducer [6].

3.1.4   Conclusion

The performance of the different current sensing techniques are compared in Table 3.1, with costs and common applications given in Table 3.2.

TABLE 3.1: Performance Comparison [6].

|	Bandwidth	DC Capable	Acuracy [%]	Thermal Drift [ppm/K]	Isolated	Range	Power Loss	Size $[mm^3]$
Shunt Resistor	kHz-Mhz	Yes	0.1-2	25-300	No	mA-A	mW-W	>25
Current Transformer	kHz-Mhz	No	0.1-1	<100	Yes	A-kA	mW	>500
Rogowski Coil	kHz-Mhz	No	0.2-5	50-300	Yes	A-MA	mW	>1000
Hall Effect	kHz	Yes	0.5-5	50-1000	Yes	A-kA	mW	>1000
Fluxgate	kHz	Yes	0.001-0.5	<50	Yes	mA-kA	mW-W	>1000
AMR Effect closed-loop,core-less	kHz	Yes	0.5-2	100-200	Yes	A	mW	>1000
Core-less open-loop GMR, AMR	kHz	Yes	1-10	200-1000	Yes	mA-kA	mW	>25
Fiber-Optivc Current Sensor	kHz-Mhz	Yes	0.1-1	<100	Yes	kA-MA	W	$>10^6$

TABLE 3.2: Application Hints [6].

	Cost[USD]	Size[mm]	Limitations
Shunt Resistor	>0.5	>25	An overcurrent can permanently damage the shunt resistor. High power losses make it difficult to measure high currents In high voltage applications the missing electrical isolation is a problem.
Current Transformer	>0.5	>500	A DC offset may saturate core material. For high currents a large core cross sectional area is required to avoid saturation. In high voltage application the winding isolation becomes crucial. A high winding ratio leads to increased parasitic capacitance, which reduces measurement bandwidth and common node noise rejection
Rogoswki Coil	>1	>1000	The accuracy depends on the conductor position. Difficult to measure small currents due to poor sensitivity. A high number of turns reduces the measurement bandwidth.
Hall Effect (open-loop/closed-loop)	>4	>1000	AC currents with high frequency can overheat the core material. An overcurrent incident does introduce a magnetic offset that can only be eliminated with a degaussing cycle. Distinct thermal drift that has to be compensated.
Fluxgate	>10	>1000	Some variants induce notable voltage noise into the primary winding. Complicated control electronics. A high number of turns reduces the measurement bandwidth
AMR Effect(closed-loop,core-less)	>5	>1000	Not practical for very high current since the current has to flow trough the sensor housing. Susceptible to external magnetic stray fields. Bandwidth limited to <1 MHz
Core-less,open-loop	>2	>25	Highly sucepitble to external magnetic fields. If the sensor is close to the current carrying conductor, the skin effect may limit the frequency response
Fiber Optic current Sensor	>1k	$>10^6$	Due to high complexity not suitable to measure small currents. Bending stress of the fiber-optic cable deteriorates the accuracy.

Shunt resistors may have a good accuracy, are one of the simplest techniques and therefore are widely used to measure currents on printed-circuit-boards. At higher currents, this technique becomes troublesome due to high power losses.

On the other hand, Hall effect current sensors provide galvanic isolation, high bandwidth and good accuracy. These sensors are commonly used in different application like automotive, industrial, space, or energy distribution. Closed-loop AMR based current sensors are very similar to Hall effect sensors with the advantage of being more sensitive although they are more costly.

For highest performance, fluxgate are used but due to their high price are only suitable for very specialized applications. For very high direct current, fiber optic current sensors are used.

Current transformers and Rogowski coils are popular techniques for measuring alternating currents and generally used in power distribution. These techniques provide high accuracy and galvanic isolation and can be used to measure currents from amperes up to mega amperes at a very low cost.

Core-less and open-loop magnetic field sensors are able to sense current at low bulk and reasonable price. However, the accuracy may be low due to the skin effect and are sensitive to external magnetic field that are difficult to shield.

3.2   Applicable Technology

Having introduced the techniques to measure electrical currents and the needed conditions to make them space qualified, it is time to focus on which techniques are the most suitable based on the project requirements.

Requirement R07 specifies that the sensor must measure the DC component of the input signal, in addition with requirement R05, which specifies the measurement bandwidth, the sensor must be able to sense AC and DC components. With help of Table 3.1, current transformers and rogowski coils are excluded, as they are not capable of sensing DC components of a signal.

Requirements R13 and R14 specify mass and volume minimization respectively, therefore excluding Fiber Optic current sensors, as they can be very large and with applications to sense currents with Kilo to Mega Amperes of magnitude.

Fluxgates are very complicated devices, they are usually designed for a specific scenario, making them very difficult to find COTS for a specific problem.

Thus we are left with: shunt resistors, Hall effects, GMR and AMR sensors.

3.2.1   Hall Effect

Hall effect current sensors are traditionally in the airgap of a magnetic core to increase accuracy. This leads to sensing errors: sensitivity to close currents due to the magnetic leakage associated with the airgap (necessary to accommodate the sensor) and DC errors caused by the hysteresis of the magnetic core. Furthermore, magnetic cores will increase the sensor size and mass. Regarding magnetic technologies, Hall sensors seem to be more sensitive to radiation damage than AMR sensors [8]. For low field environments, AMR and GMR sensor have the advantages of higher sensitivity, wider frequency range, smaller size, lower power consumption and relatively low cost[11].

3.2.2   AMR and GMR

AMR and GMR sensors are technologies that have recently been launched to space. AMR sensors from manufacturer *Honeywell®* have been used in the the Spanish NANOSAT (2004) , the Norwegian NCubes (2005), the Japanese CUTE 1.7 (2005) and the American ION (2005)[8]. GMR sensor from manufacturer *NVE®* have been flown in triple-cubesat called OPTOS [12]. These are in the highest level of technology maturation and are therefore space qualified.
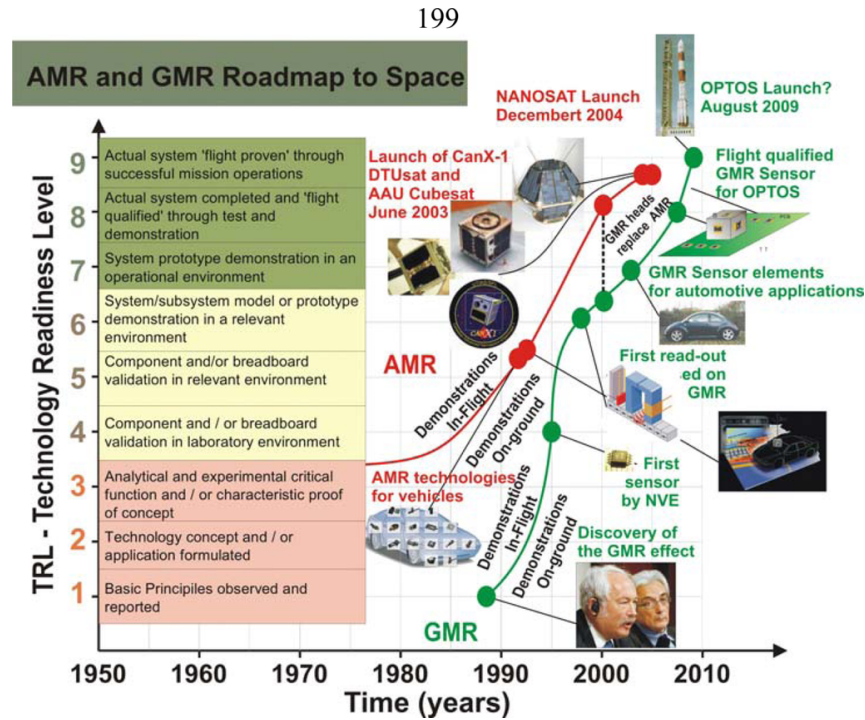
FIGURE 3.13: Space validation of GMR and AMR technology [13].

The following table resumes some magnetic properties and the approximate price of AMR and GMR commercial magnetic sensors suitable for space applications.

TABLE 3.3: Magnetic properties and approximate price.

Technology	COTS	Magnetic Field Range (μT)	Resolution (nT)	Noise Density (nT/$\sqrt{Hz}$)	sensivity (mV/mT)	BW	Mass(g)	Price(€)	Observations
AMR	HMC1021	±600	8.5 @ 5V and 1Hz	1 @ 1Hz	50 @ 5V	DC-5Mhz	<0.5	24	Manufactured with Barber Pole biasing
GMR	ALL002	1,5	10 @ 5V and 1Hz	1 @ 1Hz	175 @ 5V	>1MHz	<0.5	7	Needs biasing

GMR technology have greater resolution, sensitivity and lower noise than the AMR. Nevertheless, this GMR sensor is unipolar, meaning it can not sense the magnetic fields direction, making it a handicap. Whereas the AMR is more limited in magnetic properties, but has the advantage of being bipolar as a result of barber pole biasing, as explained in Section 3.1.

3.2.3 Shunt Resistors

Shunt resistors have the advantage of being the simplest technique to sense a electrical current and with a well calibrated resistor, good results can be achieved. Requirement R9 establishes the power consumption of the sensor and, as shown before, this technique has the drawback of dissipating a great deal of power. Shunt resistors are the technique currently in use at the Solar Power Regulator of Active Space, so it is experimental results will be later compared with the new sensor being designed. Some manufacturers of space grade precision resistors are *Isabellenhuette*® and *Vishay*®.

3.3   COTS applicable

In conclusion, it was chosen to use AMR technology in face of GMR, as AMR is less sensitive but provides bipolar sensing without the need of biasing coils. *Honeywell®* offers two one axis magnetic sensors which are listed in the table below.

Characteristics	HMC1001	HMC1021S	Conditions	Units
Supply	5.0 to 12.0	2.0 to 25	Vbridge (Vb) referenced to GND	Volts
Field range	±2	±6	Full scale (FS) total applied field	gauss
Linearity Error	1.0	1.6	Best fit straight line at max field range	%FS
Bridge Offset	-15	±2.5	Offset = (OUT+) (OUT-)Field = 0 gauss after Set pulse, Vb = 8V	mV
Sensivity	3.2	1.0	Set/Reset Current = 3A	mv/V/gauss
Noise Density	29	48	@1Hz, Vb=5V	nV/sqrt Hz
Resolution	27	85	10Hz Bandwidth, Vb=5V	micro gauss
Bandwidth	5	5	Magnetic signal (lower limit = DC)	Mhz
Disturbing Field	5	20	Sensitivity starts to degrade.Use S/R pulse to restore sensitivity.	gauss
Sensitivity Tempco	-0.30	-0.30	TA= -40 to 125řC, Vb=8V	%/C
Bridge Offset Tempco	±0.03	±0.05	TA= -40 to 125řC, Vb=8V	%/C
Max. Exposed Field	10000	10000	No perming effect on zero reading	gauss

TABLE 3.4: Characteristics of HMC1001 and HMC1021S sensors

The *Honeywell®* HMC100X and HMC102X AMR sensors are simple resistive Wheatstone bridges to measure magnetic fields and only require a supply voltage for the measurement. With power supply applied to the bridges, the sensors convert any incident magnetic field in the sensitive axis directions to and outputs a differential voltage. In addition to the bridge circuits, each sensor has two on-chip magnetically coupled straps: the offset strap and the set/reset strap. These straps are *Honeywell®* patented features for incident field adjustment and magnetic domain alignment and eliminate the need for external coils positioned around the sensors.

The offset strap is a spiral of metallization that couples to the sensor elements sensitive axis. The offset strap has some modest resistance and requires a moderate current flow for each gauss of induced field. The straps will easily handle currents to buck or boost fields through the linear measurement range. Therefore they are a powerful feature to use in closed loop topologies [14].

The set/reset strap is another spiral of metallization that couples to the sensor elements easy axis (perpendicular to the sensitive axis on the sensor die). Each set/reset strap has a low resistance with a short but high required peak current for reset or set pulses. A set pulse is defined as a positive pulse current entering the Set/Reset strap connection. The successful result would be the sensor aligned in a forward easy-axis direction so that the sensor bridges polarity is a positive slope with positive fields on the sensitive axis result in positive voltages across the bridge output connections. A reset pulse is defined as a negative pulse current entering the Set/Reset strap connection. The successful result would be the sensor aligned in a reverse easy-axis direction so that sensor bridges polarity is a

negative slope with positive fields on the sensitive axis result in negative voltages across the bridge output connections. Typically a reset pulse is sent first, followed by a set pulse a few milliseconds later. The reasons to perform a set or reset on an AMR sensor are: To recover from a strong external magnetic field that likely has re-magnetized the sensor, to optimize the magnetic domains for most sensitive performance, and to flip the domains for extraction of bridge offset under changing temperature conditions.[14]

The magnetoresistive sensors are made of a nickel-iron (Permalloy) thin-film deposited on a silicon wafer and patterned in a barber pole structure, as described in Figure 3.14.
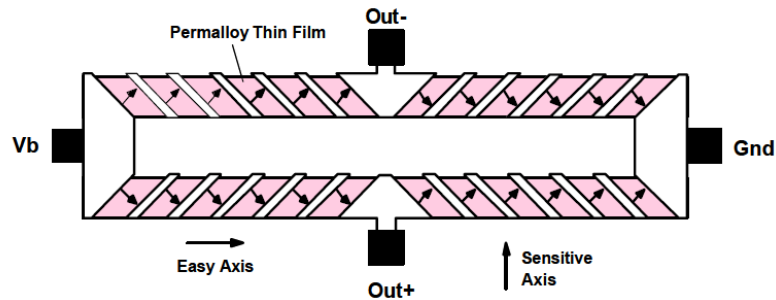

FIGURE 3.14: Magneto-Resistive Wheatstone Bridge [14]

3.4 Simulation Setup

Electromagnetic theory has been studied for centuries, being a substantiated and solid theory that provides a further understanding of our world. With the increase over the years of computation performance, it is possible to run mathematical models of the theory in a computer and to reproduce real world effects. Simulation opens a window for understanding phenomena before experimental studies or even in situations that cannot be approached experimentally. Once a problem is defined, it is easy to change parameters and run the simulation algorithm again, to understand what can or cannot be approached experimentally.

The development of a final 3D model was supported by a 2D Model. With this strategy it is possible to run several simulations and get an approximated solution which can then be extruded to a 3D model, that is to say, a more realistic one. All the simulations were performed using a Finite Element method software, *COMSOL* Multiphysics ®.

3.4.1 2D Model

This model has as it is main goal the measurement of the magnetic field generetad by the input current in the vicinity of the magnetic sensor place. To do so, a PCB with 2 copper traces with 10 amperes of current each is modelled. The physics used in this model are Magnetic Fields (AC/DC Module) with a stationary domain study type.

Geometry and Materials

The model geometry is constituted by a circle and 3 rectangles. The circle material is air and has a radius of 50 mm with a layer of 15 mm. It defines the domain surrounding the PCB.

The PCB dimensions were chosen in accordance with a standard PCB with 4 layers from PCB manufacturer, Eurocircuits. Thus, having a width of 35mm and height of 1.55mm. The material used for this object was FR4, a common material used in PCB manufacturing.

Material	Electrical Conductivity(σ)	Relative Permeability(μ_r)	Relative Permittivity(ϵ_r)
Air	0 [S/m]	1	1
FR4	0.004 [S/m]	1	4.5
Copper	5.998×10^7 [S/m]	1	1

TABLE 3.5: Properties of the materials used in the 2D simulation.

Finally, the current traces are made of copper in the computer model. For their dimension the ECSS standard for design rules for printed circuit boards(ECSS-Q-ST-70-12C) was given a special attention. In Chapter 13 - Electrical requirements for PCB design, section 13.6 Current rating and subsection 13.6.2 - Requirements for temperature increment, specifies:

- The temperature increment of tracks with respect to the dielectric substrate shall be 10 °C.

- The temperature increment of tracks with respect to the dielectric substrate should be 5 °C.

- The temperature of tracks shall be 95 °C.

- The temperature of tracks should be 85 °C.

The standard gives 3 experimental models for calculating current rating and cross sectional area, and they are given by the following formulae:

$$I = k_0 \Delta T^{k_1} \left(c_1 A \right)^{m_0 \Delta T^{m_1}} , \tag{3.6}$$

$$A = \frac{1}{c_1} \left(\frac{I}{k_0 \Delta T^{k_1}} \right)^{\frac{1}{m_0 \Delta T^{m_1}}} . \tag{3.7}$$

- Current rating [I in Amp].

- Cross sectional area of tracks [A in mm^2].

- Temperature increment of tracks [ΔT in °C].

- Constants k0, k1, m0, m1. The values of the constants are specific for each experimental model.

- Conversion factor mm^2 to $mils^2$ c1=1550.

It was used the model IPC-2152, for this is the most comprehensive standard for the computation of track current rating, with the following constants [15]:

- k0 = 0,0756.

- k1 = 0.4375.

- m0 = 0.5000.

- m1 = 0.0301.

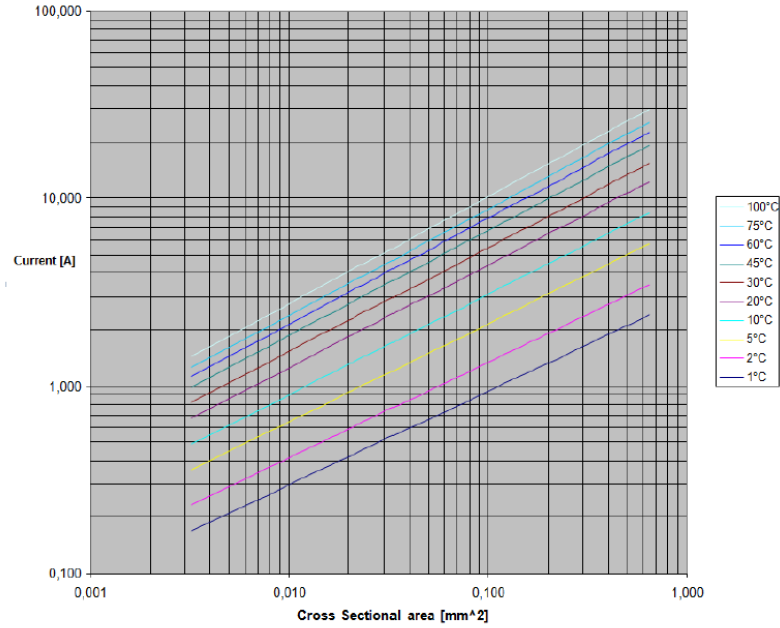FIGURE 3.15: IPC-2152: Current rating [A] vs cross sectional area $[mm^2]$ in double log scale [15].

For $I = 10A$ and $\Delta T = 10\,°\mathrm{C}$, applying Equation 3.7 leads to a cross sectional area of 0.21 μm which is commercially impracticable for a prototype. Therefore, the copper trace dimensions were chosen in accordance with PCB manufacturing prices. The least expensive corresponds to a trace height of 30 μm. The width was chosen to be $30mm$, so as to optimise a parallel field alongside the sensor sensitive axis. For future work, a pcb with several layers should be manufactured in order to decrease the current of each track and a thicker copper trace should be used to increase cross sectional area and, thus, accomplish the standard regulation.

Domain Equations

An external current density J_e is introduced in the copper traces domains,(Figure 3.16) with the following equation:

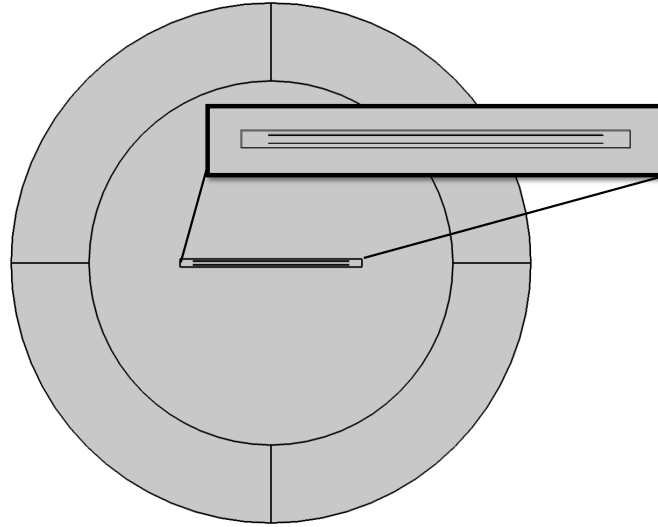$$\nabla \times \boldsymbol{H} = \boldsymbol{J_e}. \tag{3.8}$$

FIGURE 3.16: 2D model geometry with zoom in the PCB and copper trace domains.

For a given height H, width W, and electrical current I, J_e is calculated with:

$$J_e = \frac{I}{WH}. \tag{3.9}$$

Whereupon, with Ampère's circuital law, it is possible to calculate the magnetic field generated by $\boldsymbol{J_e}$

$$\boldsymbol{B} = \nabla \times \boldsymbol{A}, \tag{3.10}$$

$$\nabla \times \left(\frac{\boldsymbol{B}}{\mu_r \mu_0}\right) - \sigma \boldsymbol{v} \times \boldsymbol{B} = \boldsymbol{J_e}. \tag{3.11}$$

Boundary Conditions

The boundary condition in the boundary edge illustrated in Figure 3.17a corresponds to a zero magnetic flux through the exterior of this edge, given by:

$$\boldsymbol{n} \times \boldsymbol{A} = 0; \tag{3.12}$$

(A) Boundary Edge

(B) Infinite element domain
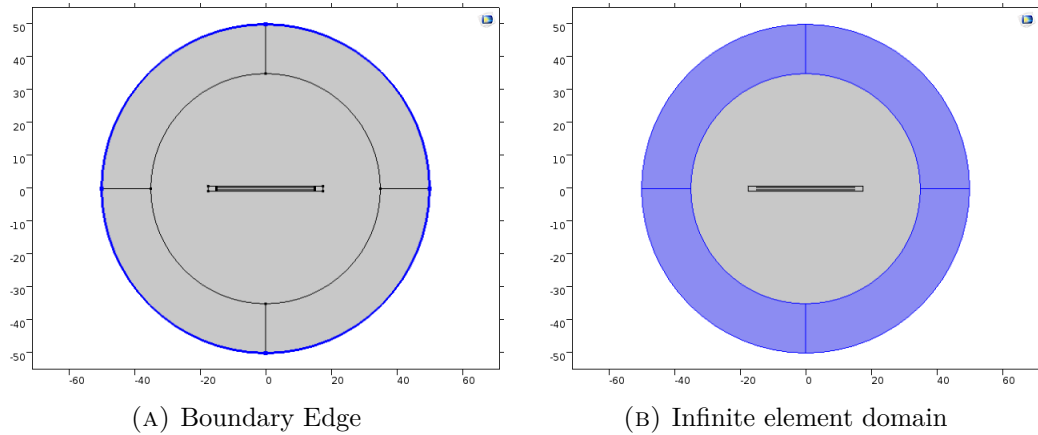
Figure 3.17: Boundary Conditions.

Obviously, it is not possible to model an infinitely large domain. The model domain must be truncated to some finite size that will give reasonably accurate results, but will not require too much computational effort to solve. However, an interesting feature from *COMSOL*®software can be used, an Infinite Element Domain. It requires the placement of an additional domain as a layer around the exterior of the modelling domain. The software then internally performs a coordinate stretching within this domain such that the domain is infinitely large, for all practical purposes. Thus, the solution from a model with infinite element domains will be the same as when the domain radius is increased. This layer is illustrated in Figure 3.17b.

Mesh

The strategy for building the mesh for this model was to first create a free triangular mesh in the domains of copper traces, PCB and air and then use a mapped one for the infinite element. To obtain the most accurate results, the mesh was built as a fine mesh. It is depicted in Figure 3.18 and consists of 26058 domain elements, 2723 edge elements and 20 vertex elements. The relative processing tolerance on the solution was set to $1 \times 10^{-}5$, which means that the computed state will be accurate to within 0.001%.
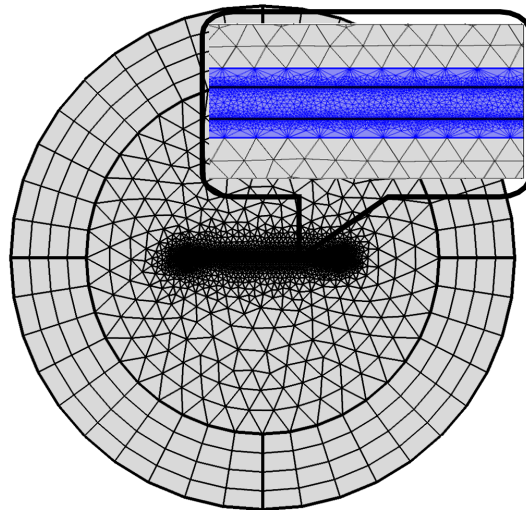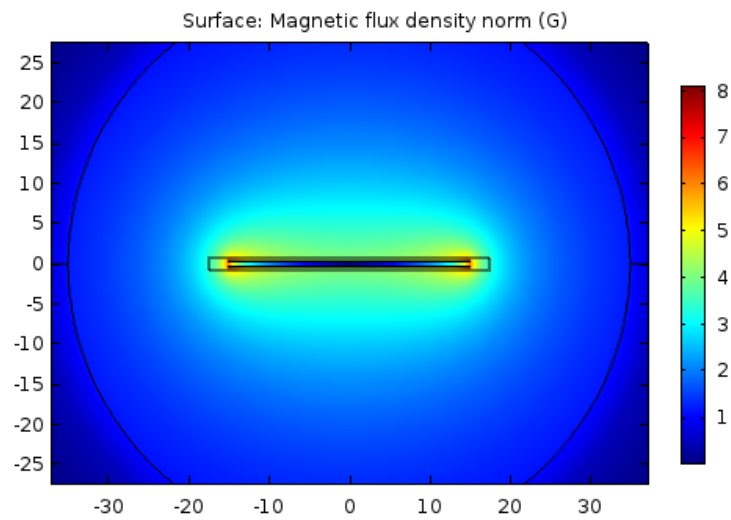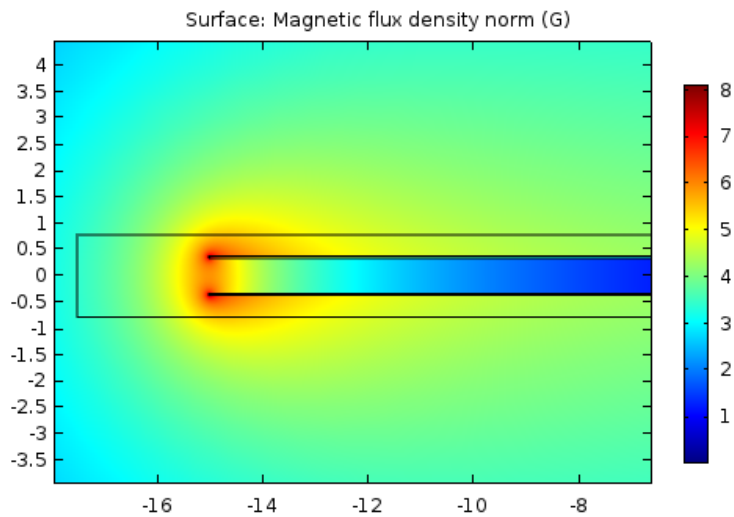
FIGURE 3.18: Mesh appearance on the 2D model. At blue, is the mesh generated in the PCB domain.

Results

(A) All domains.

(B) Closer look at copper trace and PCB domains.

FIGURE 3.19: Magnetic Flux Density Normalized.

The goal of this simulation was to understand the intensity of the magnetic flux at the place where the sensor will be soldered, however it is not in a fixed point, as it depends on soldering, chip size and PCB manufacturing. To overcome this, a measurement of the magnetic field alongside a straight line was made. This line is vertical, begins at 0.8 *mm* and ends at 2*mm* of height and it is centred in $x = 0$, as illustrated in Figure 3.20a. In practice, it means measuring the magnetic flux from the face of the PCB until 1.2mm of height.

(A) Cut line geometry.

(B) Magnetic flux density, x component alongside the cut line.
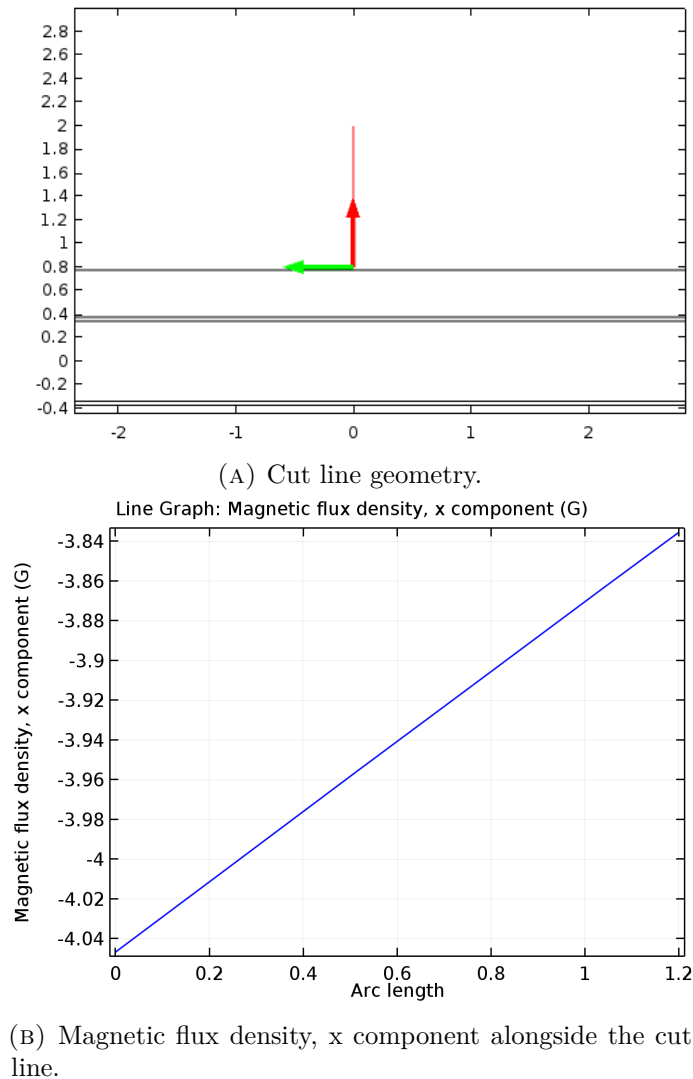
FIGURE 3.20: Cut line study.

With this result, at the sensor proximity, it will be sensing, at maximum input current, a magnetic field flux around 4 Gauss.

3.4.2   3D Model

For this model the boundary conditions and domain equations are the same as the 2D model.

Geometry and Materials

This model is very similar to the 2D model, i.e, the 2D is extruded to a 3D model. For mesh generation simplicity, the PCB domain was removed without loss of accuracy ; thus, it is left with a spherical air domain of $r = 65mm$, with a layer of $27.5mm$. The copper traces also have a height of $30\mu m$ and width of $30mm$, as in 2D, but also a depth of $50mm$. The materials are the same as in the 2D model.
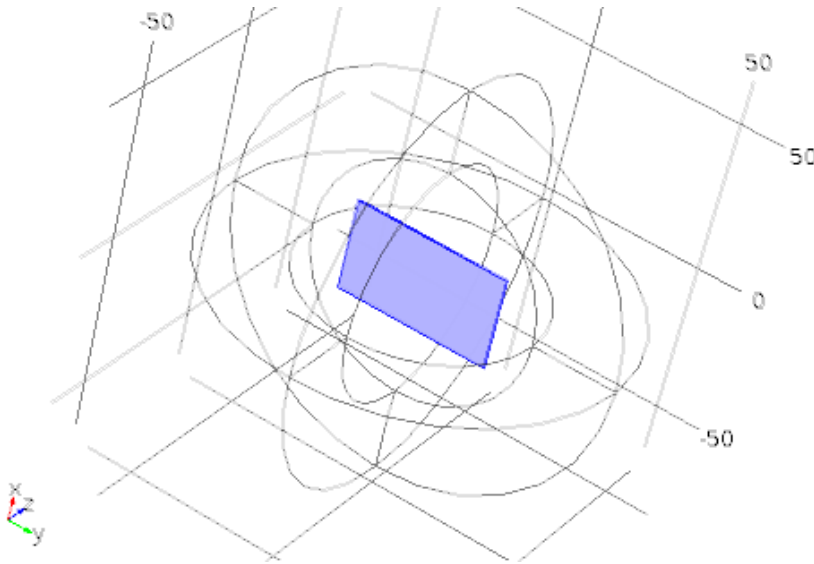

FIGURE 3.21: 3D model geometry, in blue is ilustrated the copper trace domains

Mesh

The generation of a fine mesh for this model was very difficult as the model has a high aspect ratio geometry, it has a air domain whose size in a magnitude order of mm and a copper trace with size in a magnitude order of μm, thus being very difficult to generate a fine mesh in all model. The strategy used for building the mesh was the same as the 2D, with the difference that in 3D free triangular mesh becomes free tetrahedral. The mesh is depicted in Figure 3.22 and consists of 146842 domain elements, 6424 edge elements, 16 vertex elements and average element quality of 0.1424. In general, elements with a quality below 0.1 are considered of poor quality for many applications. Having an average element quality very close to this number gives the information that our mesh has low quality.
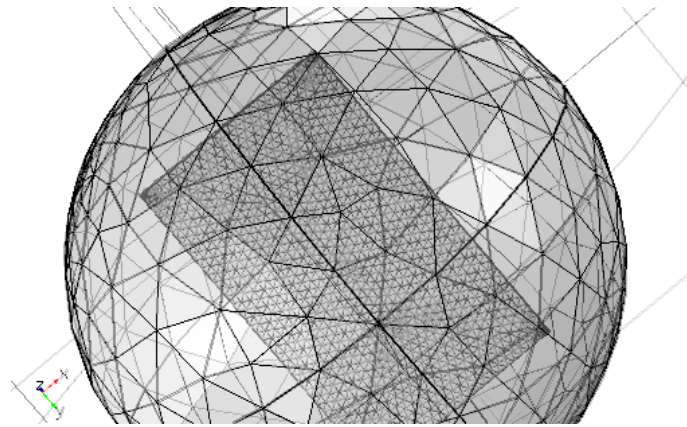
(A) Mesh in the air and copper trace domains.
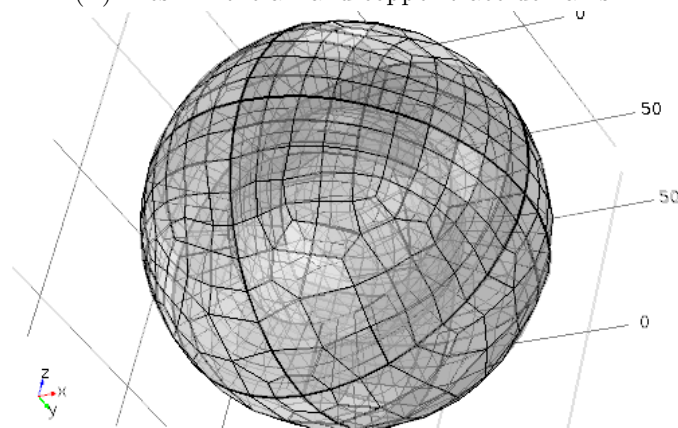
(B) Mesh in all model domains.

FIGURE 3.22: Mesh appearance on the 3D model.

Results

(A) Magnetic flux density, x component bellow PCB at $z = -2mm$.

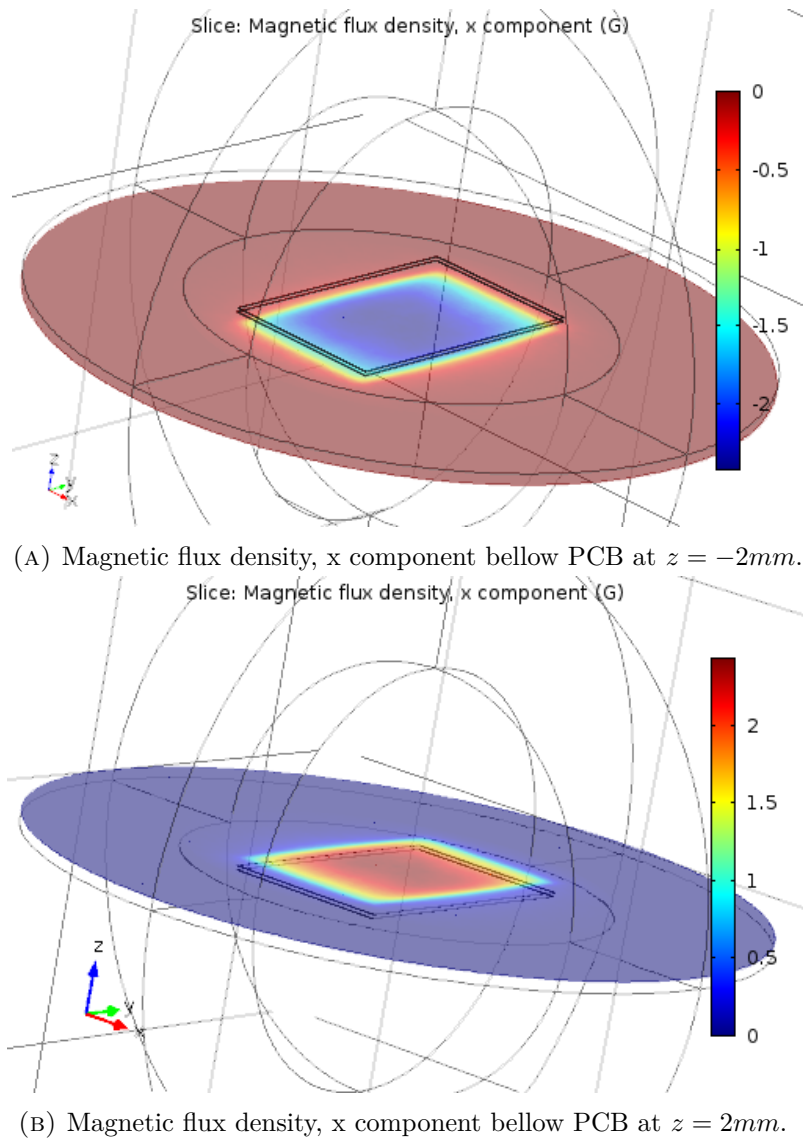(B) Magnetic flux density, x component bellow PCB at $z = 2mm$.

FIGURE 3.23: Magnetic flux density, x component study.

This model has a poor quality mesh, so to study the magnetic field alongside a line, as in the model before, it will obtain a poor quality result as illustrated in Figure (3.24).
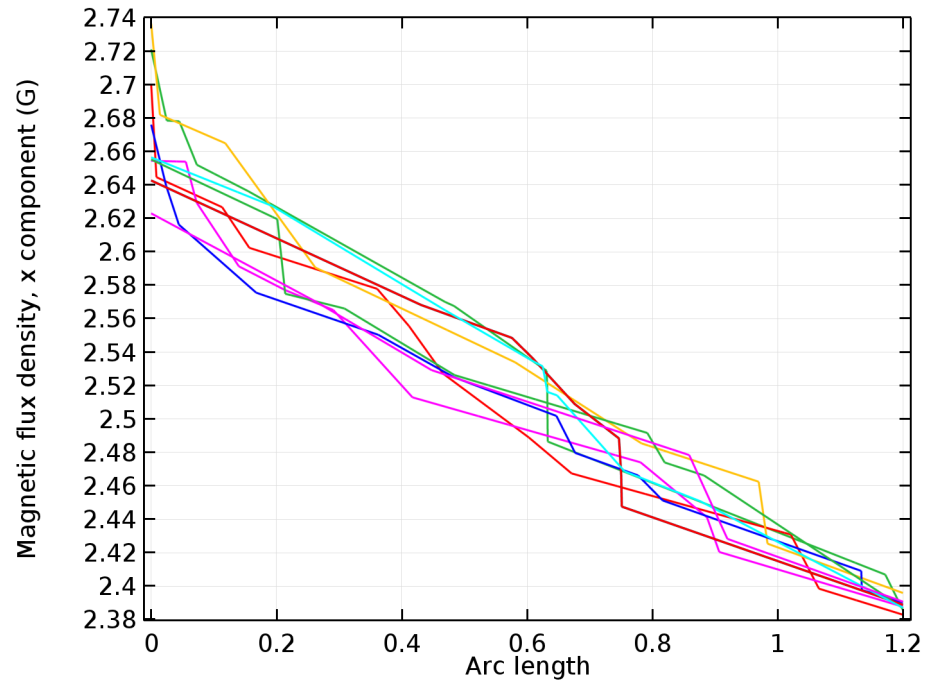
FIGURE 3.24: Magnetic Flux density, x component alongside several cut lines in different positions

In order to reach a better result, a average of several cut lines in different position was made, thus smoothing the result. Each cut line has the same length of $1.2mm$, however in a different position, but away from each other with the same distance, forming a grid. Figure 3.25 illustrates their position.
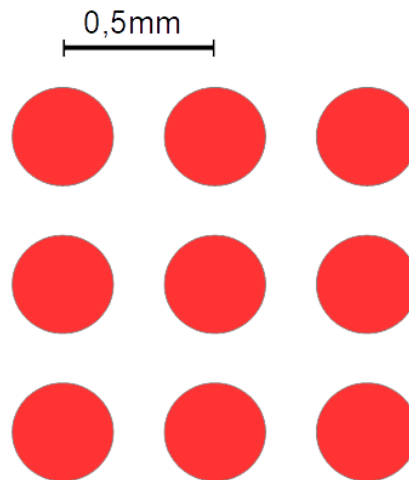

FIGURE 3.25: Cut line grid positions.

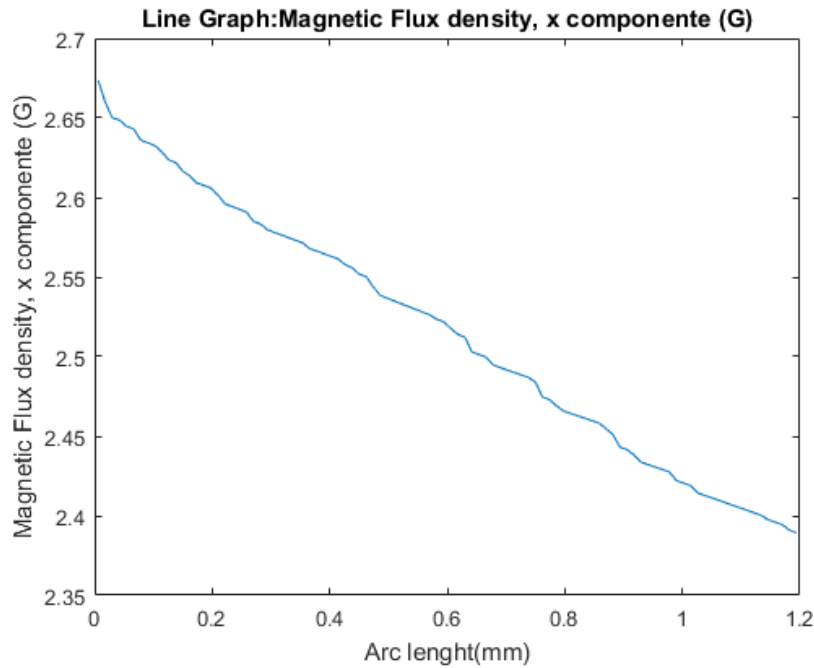The result of this strategy is given by Figure 3.26:

FIGURE 3.26: Average of 9 cut lines.

This result obtained using the 3D approach is lower then the obtained using 2D model, given the fact that in this latter case one dimension was taken as infinite.

3.4.3   Conclusion

The carried out simulations ensured the feasibility of using AMR technology as a transducer. Also given the results obtained so far, the HMC1021 as to be the one selected as magnetic fields higher then 2 gausses are to be expected.

Chapter 4

Sensor Designing

With the right transducer chosen, this Chapter describes the sensor design. In order to do so, several designs were simulated to guarantee success. The simulations were made in a SPICE simulator produced by semiconductor manufacturer Linear Technology: *LTspice*. For the PCB design, *Altium* was the software used.

4.1   Sensor Architecture

In this architecture, a closed loop topology was adopted to decrease non-linearity and thermal drift from the HMC1021. In close loop, the gain of the system is almost entirely determined by the feedback network, so thermal drifts and linearities are not dependent of the HMC but on signal conditioning electronics. The system is composed by a differential amplifier, a low pass filter, an offset driver, a set/reset driver and the HMC1021. An electric current generates a magnetic field which will be sensed by a magnetic sensor, HMC1021. At the HMC terminals the signal is measured by means of a differential amplifier, this signal has the AC component of the input signal. The HMC datasheet only gives information relative to DC signals in the offset coil, so the closed loop is only supplied with the DC component of the electrical signal. In order to do so, the differential amplifier signal is the input of an active Low-Pass filter which removes the AC component. Since is required to also sense this component of the signal, it is to be used to fit another circuit, as described bellow(Figure 4.1) later addition. Having now a DC signal, it is the input of an offset driver. The driver converts the signal in a current that will generate a contrary magnetic field in the offset coil. With this contrary field the sensor is always working at a fixed point of sensibility. This current has the information of the DC component, so it is sensed by means of a resistor, *Rsense*. From requirement R02 the output signal must have an offset of 2.50 V, meaning that when the input signal is zero, the output must be 2.50 V.
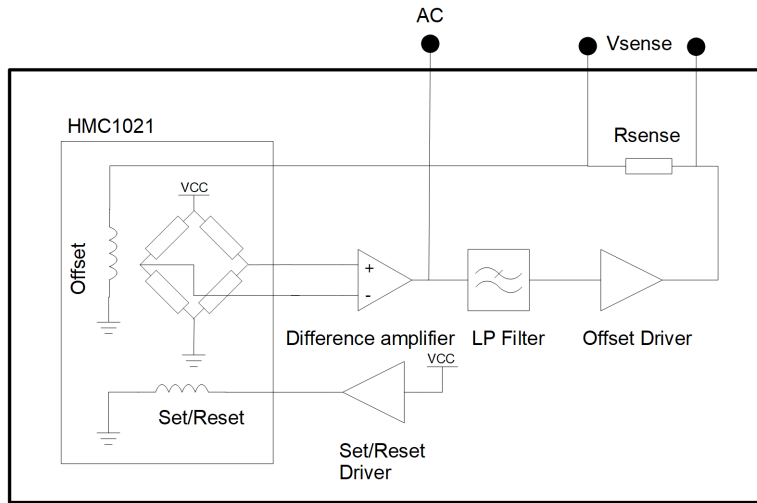
FIGURE 4.1: Sensor Architecture.

4.1.1   Low Pass Filter

It was chosen to implement a low pass filter, because there is only DC information on the current to which the offset coil must be driven. Thus, using only DC currents in the offset coil, it guarantees signal integrity. The topology used for the filter was a Sallen-key, a second-order active filter, which allows very high Q factor and can achieve high gains.
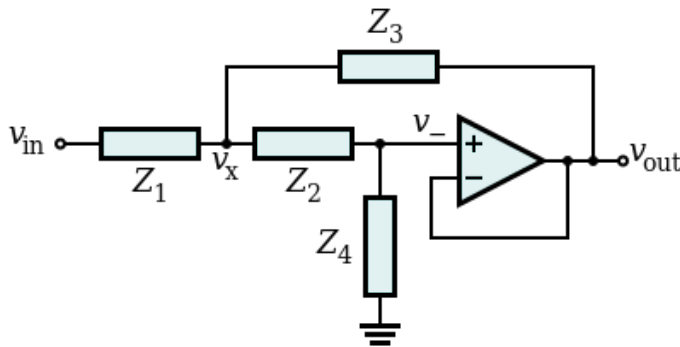

FIGURE 4.2: The generic SallenKey filter topology.

The transfer function is given by:

$$\frac{v_{out}}{v_{in}} = \frac{Z_3 Z_4}{Z_1 Z_2 + Z_3 \left(Z_1 + Z_2 \right) + Z_3 Z_4} \tag{4.1}$$

The following impedances were obtained by balancing fast step response and low corner frequency achieving 3Hz[1]:

---

[1]To calculate the impedances for a low pass filter an online tool from *OKAWA* was used: `http://sim.okawa-denshi.jp/en/OPseikiLowkeisan.htm`

- $Z_1 = Z_2 = 33k\Omega$,

- $Z_3 = Z_4 = \frac{1}{s}\mu F$,

Replacing these impedances in Equation 4.1 follows:

$$\frac{v_{out}}{v_{in}} = \frac{918}{s^2 + 60.6s + 918}, \tag{4.2}$$
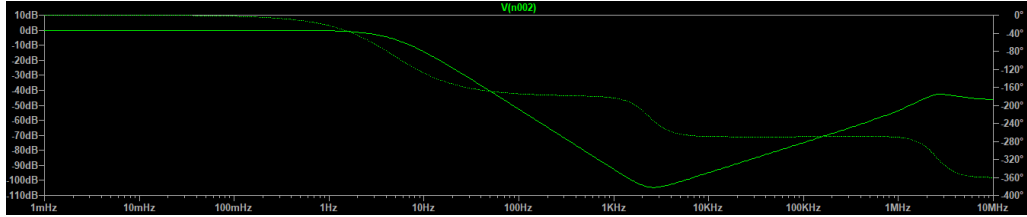

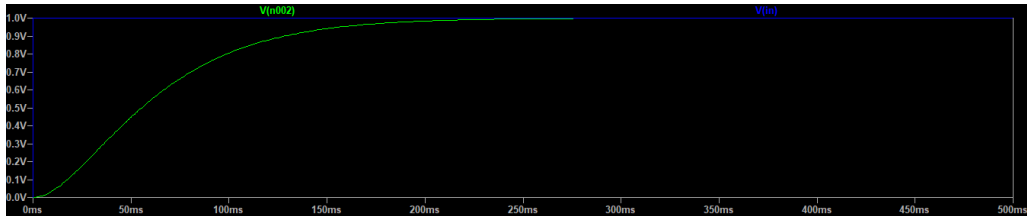FIGURE 4.3: Bode diagram for a Sallen-key with $f_c = 3Hz$.

FIGURE 4.4: Step response for a Sallen-key with $f_c = 3Hz$.

4.1.2 Set and Reset Driver

As explained in Section 3.3 a Set/Reset circuit is needed to guarantee maximum sensibility of the sensor over time. With the help of an application note from *Honeywell®* [16], a push-pull output stage was chosen.
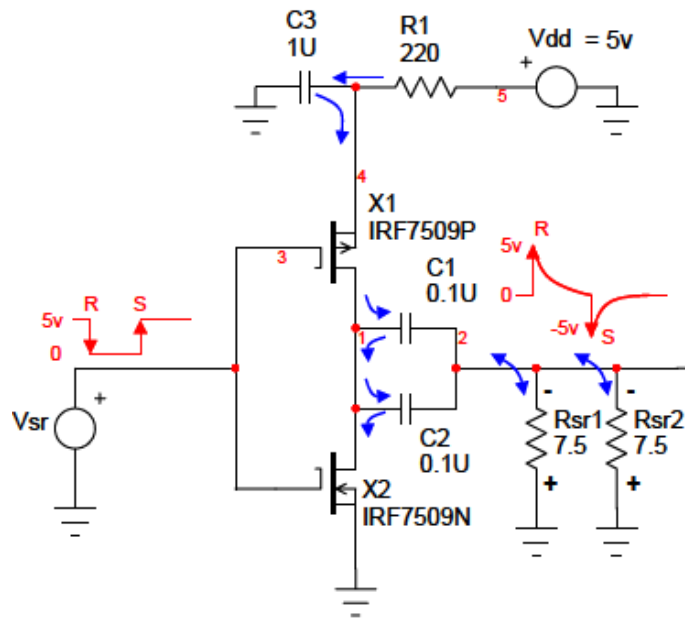
FIGURE 4.5: Set/Reset Circuit.

With the input logic voltage source (Vsr) initially held at a high logic level state (Vsr $\geqslant$ 4.5 volts), the Nchannel MOSFET X2 is fully on and effectively grounding the series circuit of C1, C2, Rsr1, and Rsr2. As the input logic source transitions to a low logic level (Vsr $\leqslant$ 0.5 volts) the MOSFET X2 turns off, thus opening up the strap resistances, while MOSFET X1 goes from its off state to its on state pulling the series R-C circuit suddenly toward the Vdd level kept by the node of X1s source and C3-R1. Again, because C1 and C2 have near zero voltage initially, the sudden pull from ground to Vdd causes all the voltage to be presented to the straps Rsr1 and Rsr2 minus any series resistance voltage drop on P-channel MOSFET X1. This becomes the reset spike and the current flows into the negative pins of Rsr1 and Rsr2.

As the reset pulse decays, capacitor C3 dumps part of its charge down through MOSFET X1 and into C1, C2, Rsr1, and Rsr2. Eventually capacitors C1 and C2 accumulate a full charge of near Vdd and C3 begins to recharge as well.

To perform the set pulse function, MOSFETs X1 and X2 flip on and off states, shutting off the Vdd source through X1 and suddenly connecting capacitors C1 and C2 to ground, creating a negative Vdd voltage across Rsr1 and Rsr2. The voltage application then creates the requisite current pulse that decays at a rate determined by the on resistance of X2 added to the paralleled strap resistances and capacitances of C1 and C2. This current pulse now flows into the positive pins of Rsr1 and Rsr2, defining a set pulse.

As the pulse current decays to zero, the sensors bridges are now at their normal factory set states, ready for measurements.[16]

4.1.3 Closed Loop Offset Driver

The offset driver's duty is to generate a current which will stimulate the coil in the transducer, generating a magnetic field which will oppose the magnetic field sensed in the transducer, leading the system in to a set point. This means that the driver will behave as an automatic controller. In order to reach a suitable driver, several designs were simulated, leading to the circuit in the figure below (Figure 4.6):
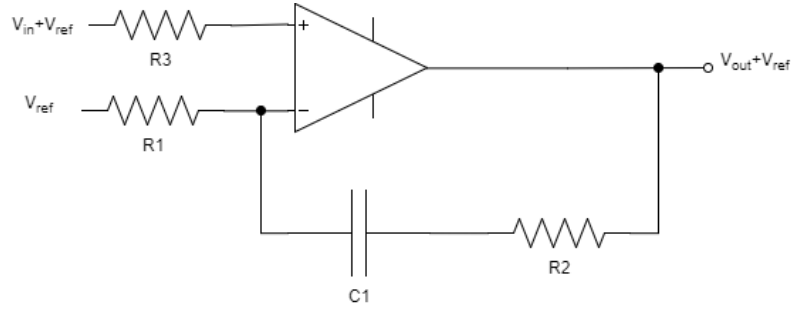

FIGURE 4.6: Schematic for the closed loop offset driver.

To start the calculation of the transfer function of the circuit, the current in the resistor R_1, I_{R1} was found:

$$I_{R1} = \frac{V_{ref} - (V_{in} + V_{ref})}{R1} \qquad (4.3)$$

As no current flows into the amplifier:

$$V_{ref} - (V_{out} + V_{ref}) = \frac{V_{ref} - (V_{in} + V_{ref})}{R1}\left(R1 + \frac{1}{sC1} + R2\right)$$

$$-V_{out} = -V_{in}\left(1 + \frac{1}{sC1R1} + \frac{R2}{R1}\right)$$

$$\frac{V_{out}}{V_{in}} = \frac{1}{sR1C1} + \frac{R2}{R1} + 1$$

$$\frac{V_{out}}{V_{in}} = \frac{1 + sR1C1 + sR2C1}{SR1C1}$$

$$\frac{V_{out}}{V_{in}} = \frac{s(R1 + R2)C1 + 1}{sR1C1}$$

$$\frac{V_{out}}{V_{in}} = \frac{s + \frac{1}{(R1+R2)C1}}{s\frac{R1}{R1+R2}} \qquad (4.4)$$

PID Controller

Proportional-Integral-Derivative controller (PID) is a control loop feedback mechanism amply used in control systems, about 90 to 95% of all control problems are solved by this controller. A PID controller continuously calculates an error value $e(t)$ as the difference between a desired setpoint and a measured process variable, and applies a correction based

on proportional, integral, and derivative terms (denoted P, I, and D respectively). [17]

The proportional controller is a simple feedback

$$u_p(t) = K_p\,e(t), \tag{4.5}$$

where e is control error, and K_p is controller gain. The error is defined as the difference between the set point, y_{sp} and the process output y, i.e.,

$$e(t) = y_{sp}(t) - y(t). \tag{4.6}$$

Proportional control normally gives a system that has a steady-state error. Integral action is introduced to remove this. Integral action has the form:

$$u_i = K_i \int_0^t e(\tau)d\tau. \tag{4.7}$$

The idea is simply that control action is taken even if the error is very small provided that the average of the error has the same sign over a long period.

Derivative control is used to provide anticipative action, as it is effectively seeking to reduce the effect of the error by exerting a control influence generated by the rate of error change. The more rapid the change, the greater the controlling or dampening effect. A simple form is:
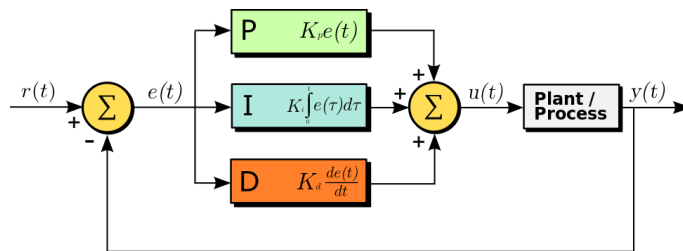
$$u_d(t) = K_d \frac{de(t)}{dt}. \tag{4.8}$$

FIGURE 4.7: A block diagram of a PID controller in a feedback loop.

The overall control function can be expressed mathematically as:

$$u(t) = K_\mathrm{p}\,e(t) + K_\mathrm{i} \int_0^t e(\tau)\,d\tau + K_\mathrm{d}\frac{de(t)}{dt}. \tag{4.9}$$

The driver circuit has some similarities with a PI Controller. To confirm this statement, $K_d = 0$ was inserted in equation 4.9 to achieve the function of a PI controller.

$$G_c(s) = \frac{U(s)}{E(s)} = K_p + \frac{K_i}{s} \tag{4.10}$$

$$= \frac{K_p\, s + K_i}{s} \tag{4.11}$$

$$= \frac{s + \frac{K_i}{K_p}}{\frac{s}{K_p}}. \tag{4.12}$$

Setting side by side 4.4 and 4.12 it is now clear that our driver behaves as a PI controller, with:

$$K_p = \frac{R1 + R2}{R1} = 1 + \frac{R2}{R1}, \tag{4.13}$$

$$K_i = \frac{K_p}{(R1 + R2)\, C1} = \frac{1}{R1\, C1}. \tag{4.14}$$

Closed Loop Tuning

Now that it is known how to calculate the PI parameters of the driver, the system must be tuned. Based on Figure 4.1 the block diagram of the overall system is represented in Figure 4.8.
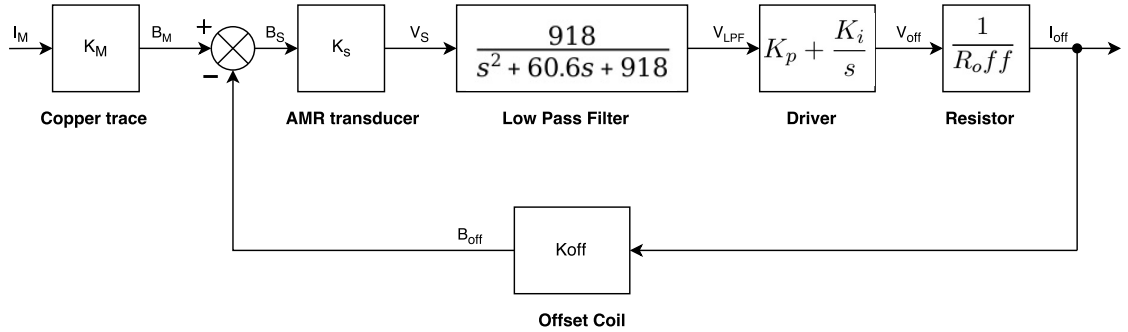

FIGURE 4.8: Block diagram of the closed-loop AMR sensor circuit.

With each variable described by:

- I_M: Current to measure(A).

- B_M: Magnetic Field due to I_M(G).

- B_{Off}: Magnetic Field due to I_{off}(G).

- B_S: Magnetic Field at AMR sensor(G).

- V_s: Transducer output voltage(mB).

- I_M: Low pass filtered V_s(mV).

- V_{off}: Offset Driver Voltage(mV).

- I_{Off}: Offset Driver Current(mV).

The control diagram from Figure (4.8) can be manipulated to obtain a PID controller diagram as in Figure 4.7 i.e, a PID controller controlling a plant/process
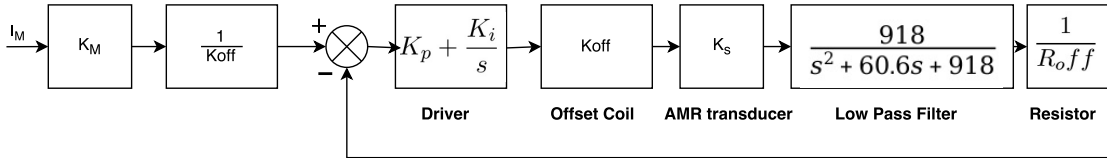

FIGURE 4.9: Block diagram of the closed-loop AMR sensor circuit in the form of a PI controller with a plant

To tune the parameters of the PI controller, a graphical programming environment for modelling, simulating and analysing multidomain dynamic systems was used, *Simulink* ®. The diagram controller from Figure 4.8 was created as a model in the software and the function PID tuner from the software package was used. The following step response was obtained :
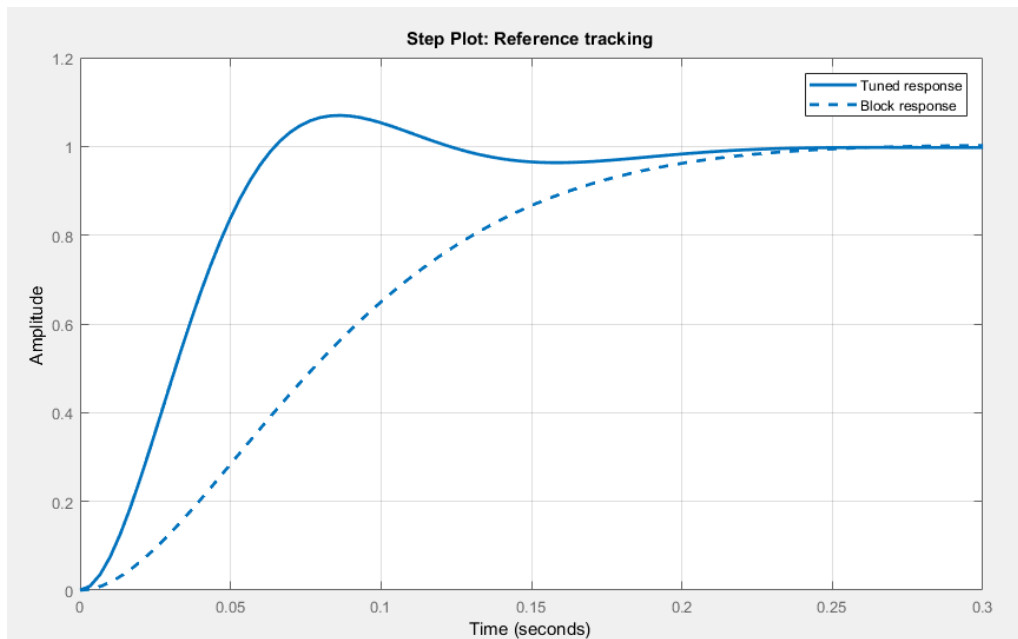

FIGURE 4.10: Step Plot from the PI controller.

The tuned response given by the auto tune algorithm is represented with the full blue line. However, it was a choice of Active Space that response speed should be sacrificed so as to avoid overshoot. Thereby, the auto tune parameters were changed in order to obtain a more robust response, given by the slashed line, thus reaching $K_P = 20.20$ and $K_I = 530.20$.

Having two Equations, 4.13, 4.14 and 3 variables to find, R1, R2 and C1, it is necessary to fix a value from one of the variables. Since it is much harder to find values of capacitance, C1 was fixed to 0.47μC, as it is very common commercial value for capacitance. This

resulted in $R1 = 4012.937\Omega$ and $R2 = 77048.390\Omega$. As these values are not commercially available, the closest ones were: $R1 = 4k2\Omega$ and $R2 = 77k\Omega$.

4.1.4 Virtual Ground

To obtain stable 2.5V from 5V a space grade zener diode was used, the RH1009 from *Linear Technologys* ®.
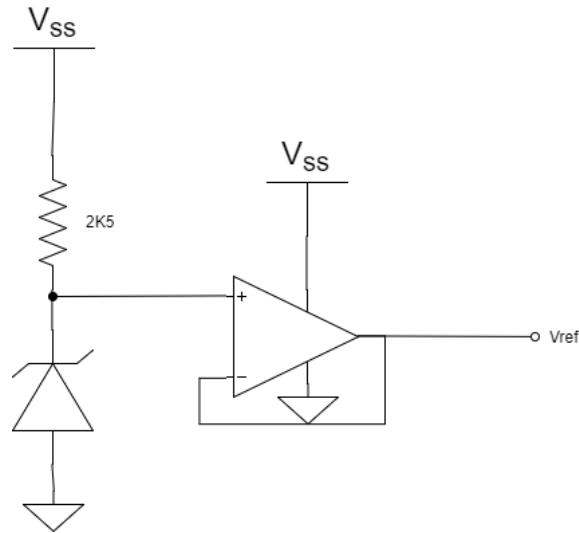

FIGURE 4.11: Electrical schematic of the virtual ground.

The resistor was chosen in accordance with RH1009 datasheet, in order to obtain a current in which the zener diode provides 2.5V. It was used an operational amplifier as a voltage follower, to guarantee that every electronic device using V_{ref} has no power limitation since is the ampop giving current to these devices.

4.2 Differential Mode Architecture

In Section 4.1 it was established the architecture and design of the transducer's signal conditioning. This architecture is not immune to external stray magnetic fields, being a possible source of errors. To mitigate this problem a differential mode was designed.
This architecture reside with two sensors sensing the same field but in opposite directions, which the output signal of each sensor is added. Thus, when a stray external field comes across the two sensors it is subtracted, as the sensing is made in opposing directions.
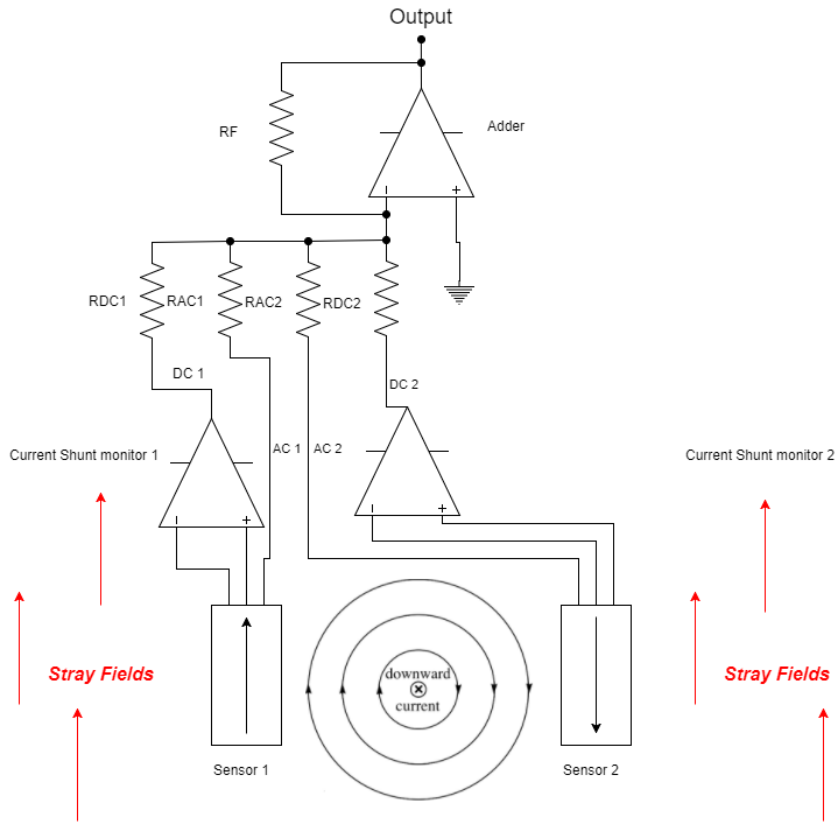The figure below illustrates this topology:

FIGURE 4.12: Differential Mode Architecture.

With Figure (4.12) it is possible to update the block digram from Figure 4.8, obtaining the following:
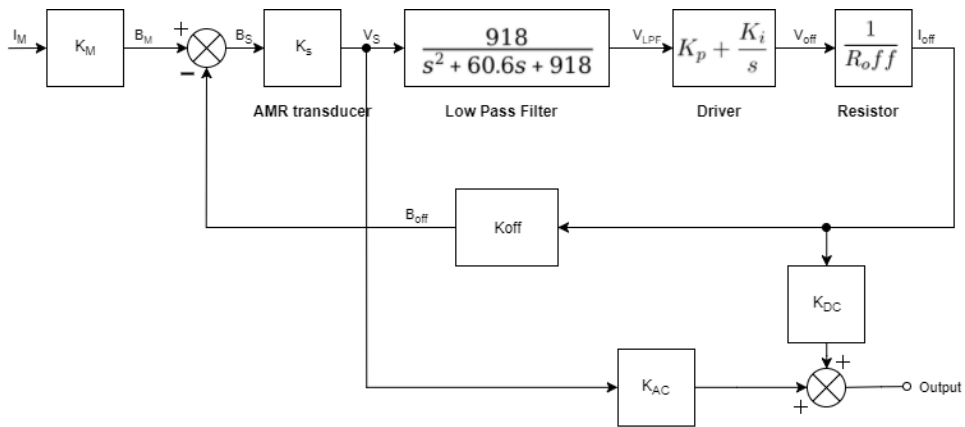

FIGURE 4.13: Block diagram of the closed-loop AMR sensor circuit with differential mode.

From requirement R02, the sensor must have an output voltage representing the instantaneous electrical current with $100 \ mV/A$. In order to do so the gains K_{DC} and K_{AC} must be calculated.

From Figure 4.13, the V_{outAC} is given by:

$$V_{outAC} = K_M\,K_S\,K_{AC}\,I_M(AC) \tag{4.15}$$

$$\frac{V_{outAC}}{I_M(AC)} = K_M\,K_S\,K_{AC}\,I_M \tag{4.16}$$

For the calculation of V_{outDC}, assuming the set point of the system is zero, it gives:

$$I_{off}\,K_{off} = I_M(DC)\,K_M \tag{4.17}$$

and knowing that V_{outDC} is given by:

$$V_{outDC} = I_{off}\,K_{DC} \tag{4.18}$$

Using equations 4.17 and 4.18, V_{outDC} is:

$$V_{outDC} = \frac{K_M\,K_{DC}\,I_M(DC),}{K_{off}} \tag{4.19}$$

$$\frac{V_{outDC}}{I_M(DC)} = \frac{K_M\,K_{DC}}{K_{off}} \tag{4.20}$$

4.3 SPICE Simulator Results

To confirm this architecture a SPICE Simulation was performed. Every electronic device was modelled with the SPICE models of the manufacturer.

4.3.1 Input Current

At first , the input current that is needed to be measured was modelled. It consists of two current sources, one generating DC current and the other generating a AC current. The AC component is a triangular signal with a frequency of 100kHz and amplitude of 1 A and the DC component is swept from 0 to 20 A. The considered current waveform is a close as possible to the one which the sensor will have to read in the PDCU from Active Space.
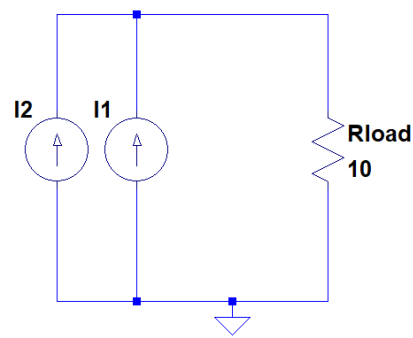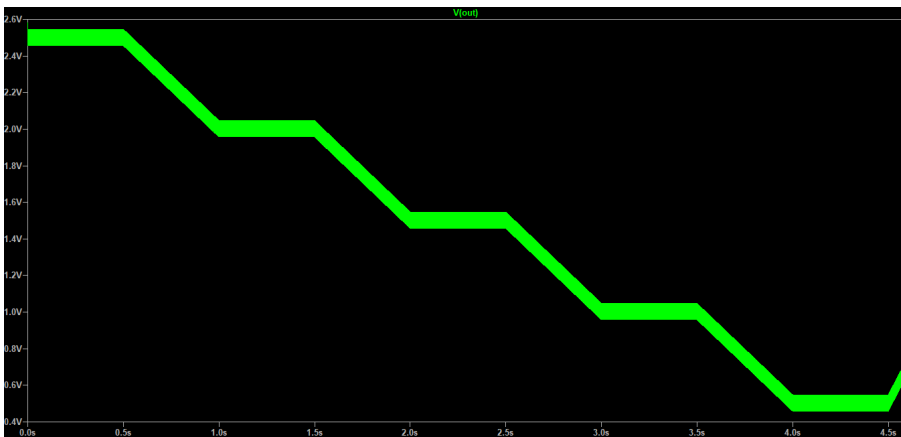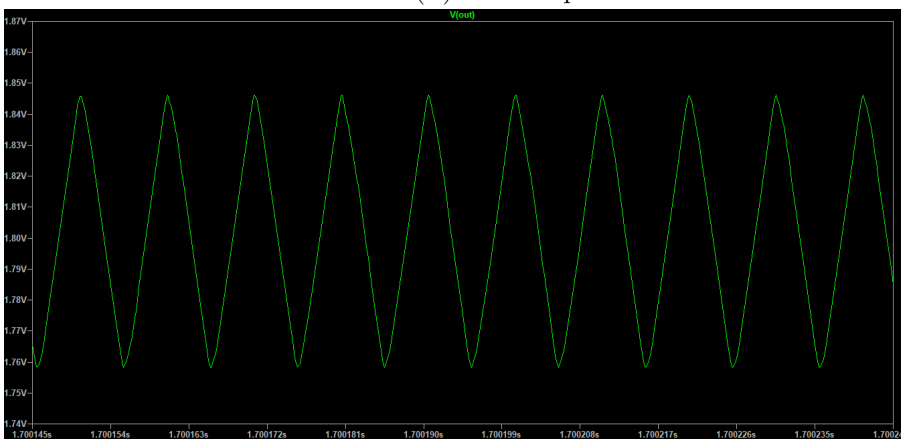
FIGURE 4.14: Model of input current.

(A) Current plot in Rload.

(B) AC component of the current in Rload.

FIGURE 4.15: Plot of the input current.

4.4   Transducer

The features of the transducer are sensibility to a magnetic field generated by the input current, external fields and the magnetic field generated by the offset strap. The HMC1021 is configured in a Wheatstone bridge in which element of the bridge is sensitive to a

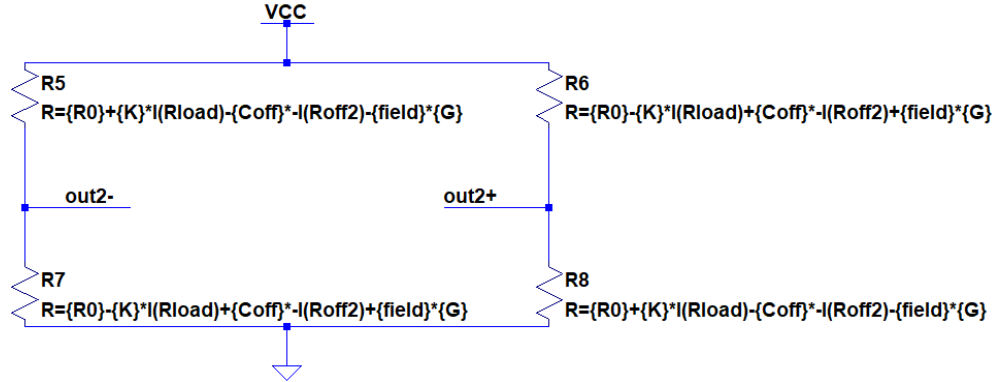magnetic field. Therefore the sensor output, it is regulated by the resistance of each resistive element.

FIGURE 4.16: Model of the transducer.

Defining V_{out} as $V_{out} = V_{out+} - v_{out-}$

Using a voltage divider to find V_{out+} and V_{out-} and subtracting one from the other, the equation for V_{out} is:

$$V_{out} = \left(\frac{R7}{R5 + R7} - \frac{R8}{R7 + R8} \right) VCC. \quad (4.21)$$

A stimulus to the transducer is equivalent to a change in resistance, to quantify it, imagine a small variation ΔR.

$$V_{out} = \left(\frac{R7 + \Delta R}{(R5 - \Delta R) + (R7 + \Delta R)} - \frac{(R8 - \Delta R)}{(R7 + \Delta R) + (R8 - \Delta R)} \right) VCC. \quad (4.22)$$

For the HMC1021 it's valid to assume $R5 = R6 = R7 = R8 = R$ with R as the typical resistance of one of the bridge elements, it follows:

$$V_{out} = \frac{\Delta R}{R} VCC. \quad (4.23)$$

Thus the fraction $\frac{R}{\Delta R}$ is equivalent to the sensibility of the transducer. From HMC1021 datasheet $R = 1100\Omega$, and sensibility is 1.0mV/V/gauss, thus $\Delta R = 1.1\Omega/mV/Gauss$. To model the sensing a magnetic field it is needed a constant which transforms the input electrical current in a ΔR. From Section 3.4 it was concluded that the constant to transform an electric current into a magnetic field is 0.15 G/A, multiplying it by 1.1 $\Omega/mV/Gauss$:

$$K_i = 0.15 \frac{G}{A} \times 1.1 \, \Omega \frac{mV}{G} = 0.165 \, \Omega \frac{mV}{A}. \quad (4.24)$$

This constant is illustrated in Figure (4.16) as K. To model the magnetic field generated by the offset current, the argument is the same as previously mentioned. The datasheet provides an offset coil constant of 4.6 mA/G, therefore:

$$K_{offset} = \frac{1}{4.6 \times 10^{-3}} \frac{G}{A} \times 1.1 \, \Omega \frac{mV}{G} = 239.13 \, \Omega \frac{mV}{A}. \quad (4.25)$$

In this case, increase in the offset current will decrease the output of the transducer, to

do so, K_{offset} is negative. This constant is illustrated in fig.4.16 as *Coff*, and is multiplied by the negative current of the offset strip in order to keep the signals integrity.

Finally the last feature is to model a presence of an external field, therefore simply multiplying an external field in gauss by 1.1 Ω. The trick of this feature when one is modelling two transducers at the same time, is that, the external field must have opposite orientation for each transducer, as we are modelling transducers with different sensing direction, as illustrated in Figure 4.12.

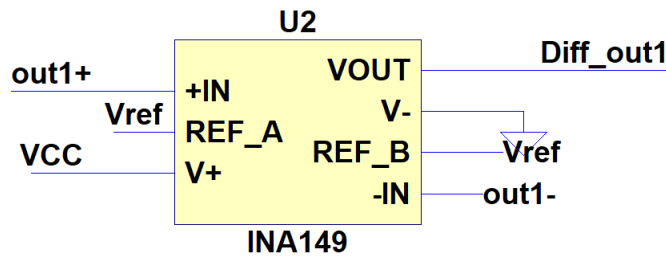### 4.4.1   Differential Amplifier

FIGURE 4.17: Model of the differential amplifier.

The following figure describes the simulated performance of the Difference Amplifier.
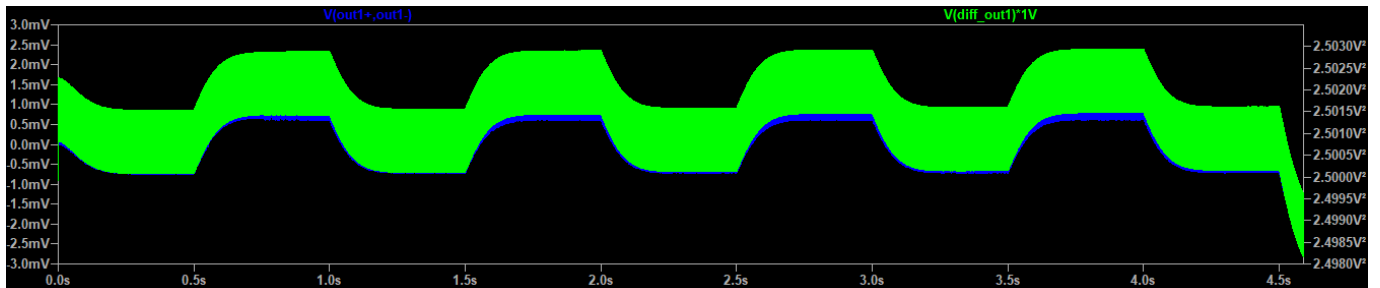

FIGURE 4.18: Input(blue) and output(green) signals of the differential amplifier.

The blue line is the difference between out1+ and out1- and the green line the output of the amplifier. The amplifier output is referenced to Vref leading to a output signal centred in Vref as required.
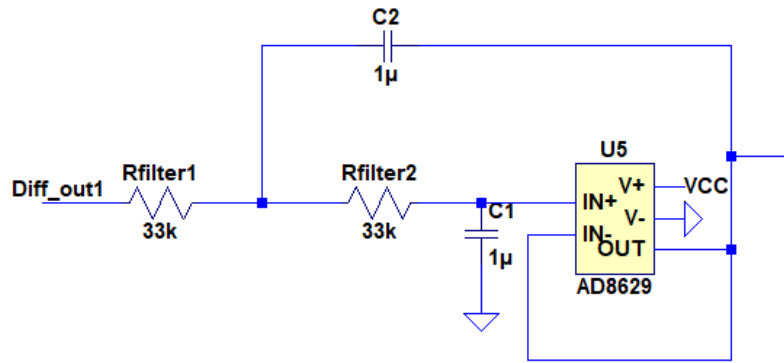
4.4.2 Filter

FIGURE 4.19: Model of the filter circuit

The following figure as in green the input of the filter and in blue the output of the filter. It's clear from the that the filter is fulfilling is requirements.
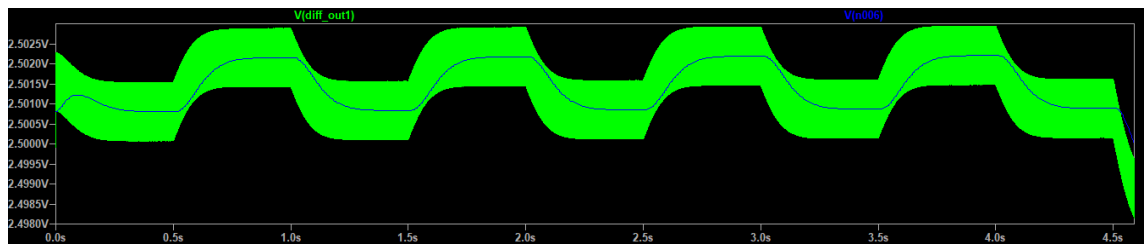

FIGURE 4.20: Input(green) and Ouput(blue) signal of the filter circuit
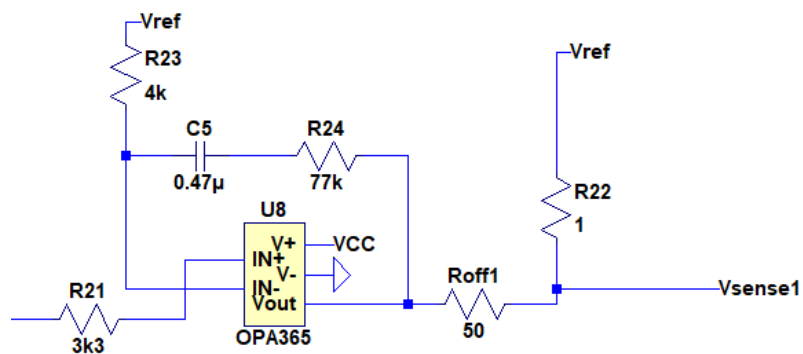
4.4.3 Offset Driver

FIGURE 4.21: Model of the Offset driver circuit

Figure 4.22 illustrates the PI controller over time. It is curious to note, despite the input being smooth, the PI reacts generating pulses of current.
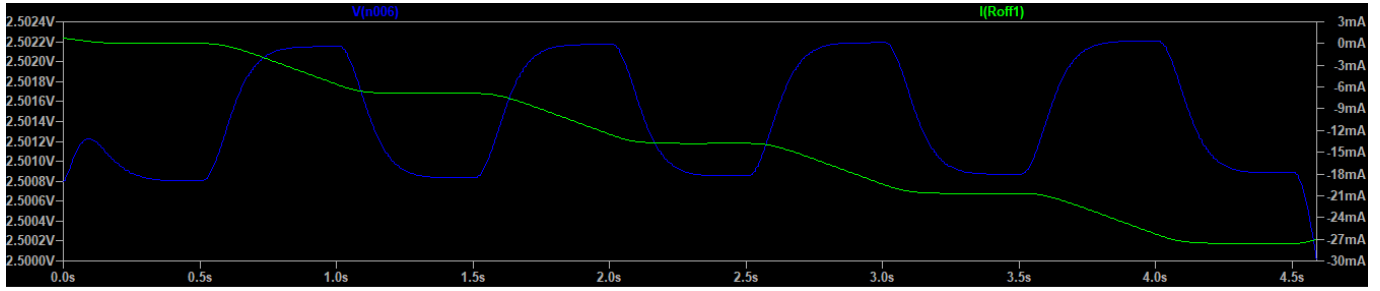
FIGURE 4.22: Input(Blue) and Output(green) signal of the offset driver circuit

.

4.4.4   Current shunt monitor
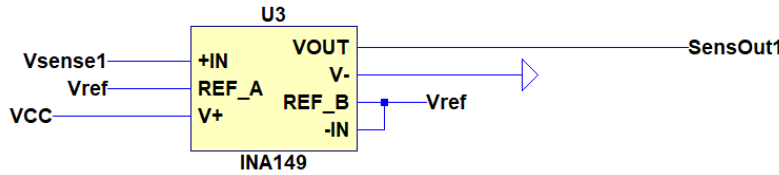
FIGURE 4.23: Model of the Current shunt monitor

Since the amplifier used as current shunt monitor is the same as the differential amplifier, it's is expected to behave well as shown in Figure 4.24.
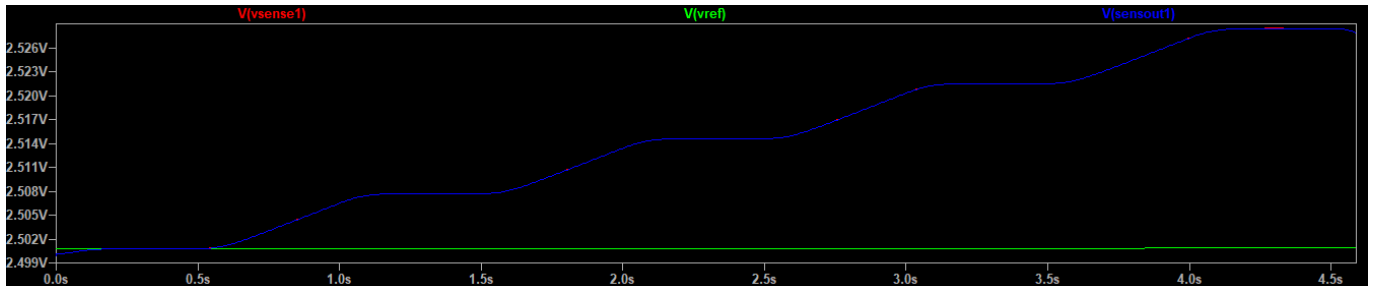
FIGURE 4.24: Model of the Difference amplifier

4.4.5   Adder

The last stage of the sensor is the adder, where two transducers and respective signal conditioning meet. The results shown in Figure 4.27 are in accordance with the calculations and models made until this stage. The output as the same waveform as the input with the right sensibility of 100mv/A. In theory, leading to a successful design,
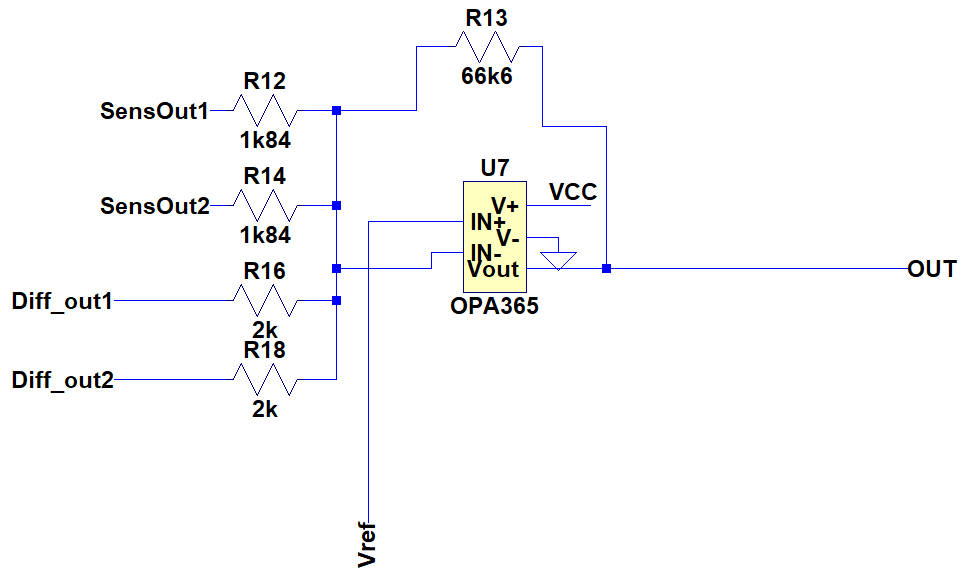
FIGURE 4.25: Model of the Adder circuit
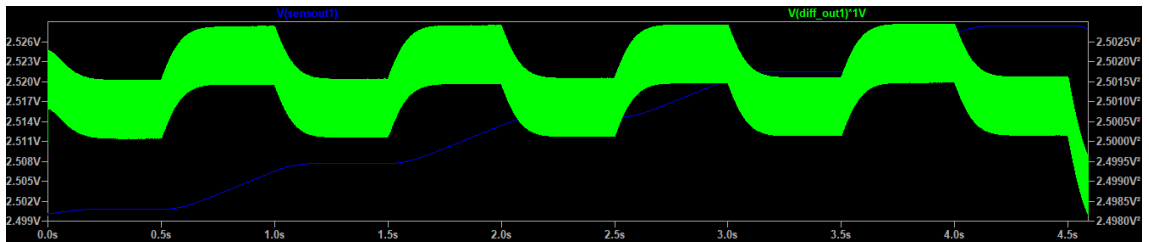
FIGURE 4.26: Adder input of one transducer
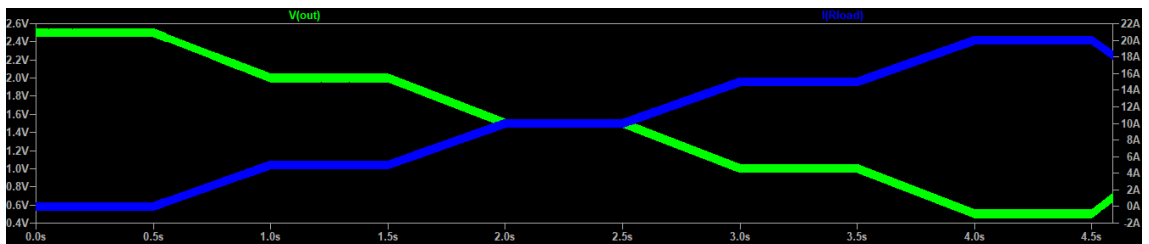
FIGURE 4.27: Adder output with input current illustrated (green)

4.4.6   Voltage Reference & VCC
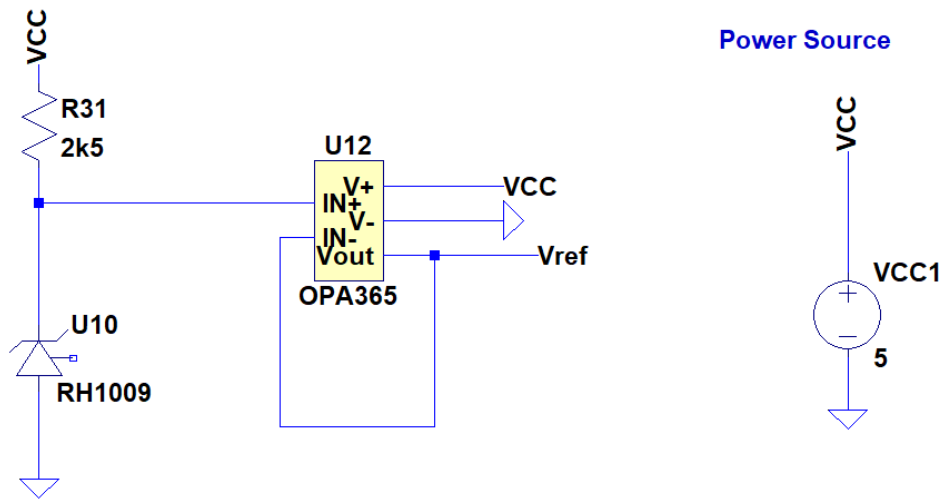
FIGURE 4.28: Model of the Voltage reference circuit and VCC

The following graphic illustrates the variation in time of the voltage reference circuit. From the figure it is possible to conclude that Vref depends on the input current, however the variation of Vref with the input is in the order of μV. Therefore this variation is negligible and it can be considered stable output over time.
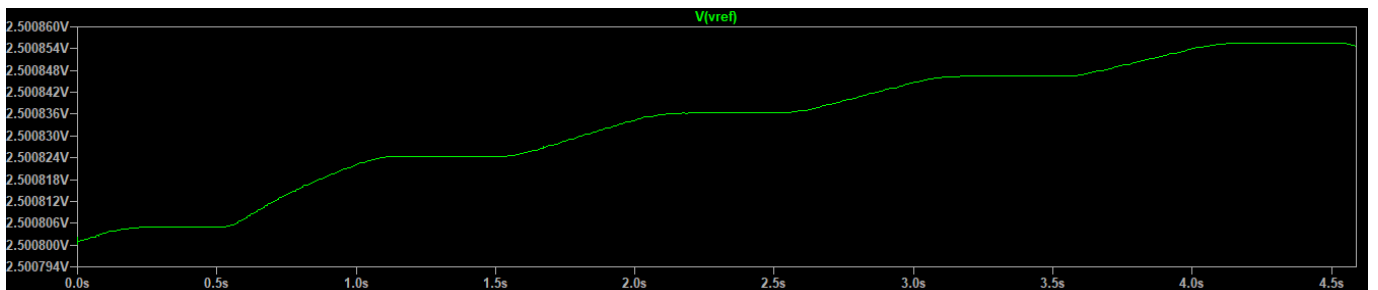
FIGURE 4.29: Output of the voltage reference circuit

Chapter 5

Testing and Results

The SPICE modelling tool demonstrated the sensor's performance in a simulated environment and now it is time to test it in real world conditions. To do so, a test bench was setup consisting of a shunt resistor with a AD8418 current sense amplifier, a current source and a PXI-1036 chassis from National Instruments. Tests were carried out using the shunt resistor as reference to the test. A current was generated by the source, which could be selected as either a DC or a AC + DC current, depending on the test that would be carried out. Then this current was sensed by both the resistor and the sensor under test. The output of each of them could be read by the PXI and data was saved in the PC for later analysis. The structure of the test bench is illustrated in Figure 5.1.
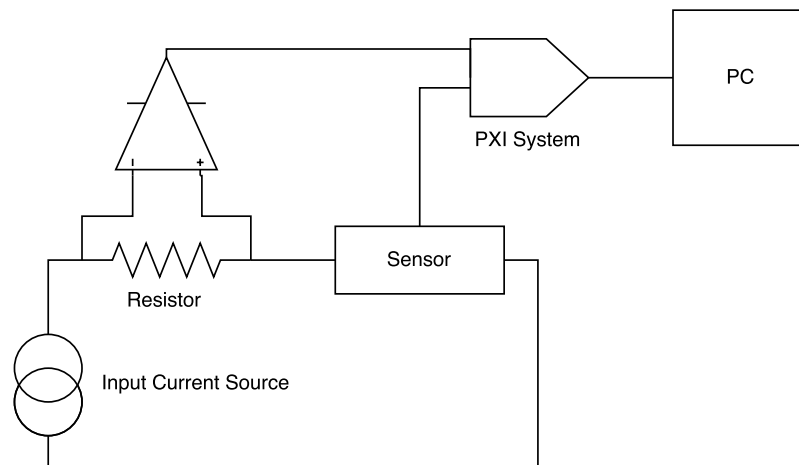
FIGURE 5.1: Block diagram representing the setup used for testing

5.1 DC Test

The input current for this test is purely DC and it will be generated from -20 to 20 A, thus, it is possible to test the sensor linearity.

Figure 5.2a illustrates the sensor output in regard to the current, whose range is from 0 to 20 Amperes. At 15 A a curious anomaly occurs, for better analyses a Savitzky-Golay

smoothing filters was used in the data.

Savitzky-Golay smoothing filters (also called digital smoothing polynomial filters or least-squares smoothing filters) are typically used to "smooth out" a noisy signal whose frequency span (without noise) is large. In this type of application, Savitzky-Golay smoothing filters perform much better than standard averaging FIR filters, which tend to filter out a significant portion of the signal's high frequency content along with the noise.

Applying this filter, Figure 5.2b was achieved. With this plot it is clear that the sensor loses linearity at 15 A. After some debugging, it was found that the operational amplifier in the voltage reference circuit, does not provide the current necessary to maintain a stable closed loop with a input current of this magnitude.
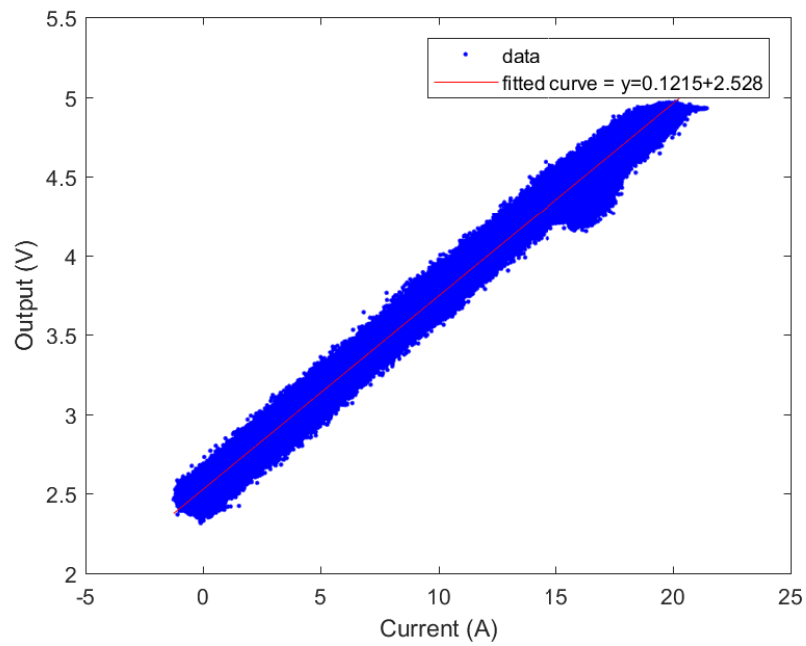
(A) DC test from 0 to 20 A with fitted curve
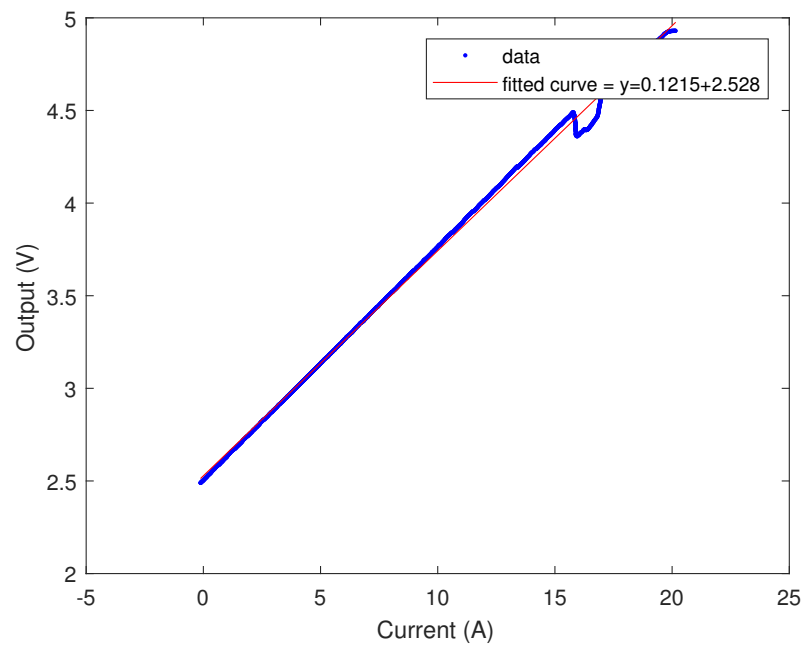
(B) DC test from 0 to 20 A with fitted curve filtered

From the input range of -20 to 0 A, the same anomaly occurs in a more subtle way, however the sensor at this range also loses linearity at -15 A. This is represented in Figures 5.3a and 5.3b
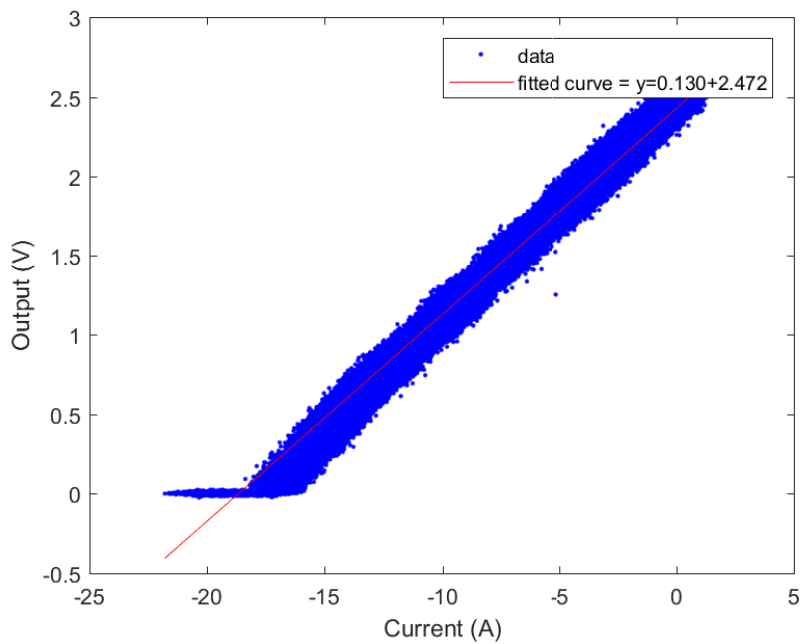
(A) DC test from -20 to 0 A with fitted curve
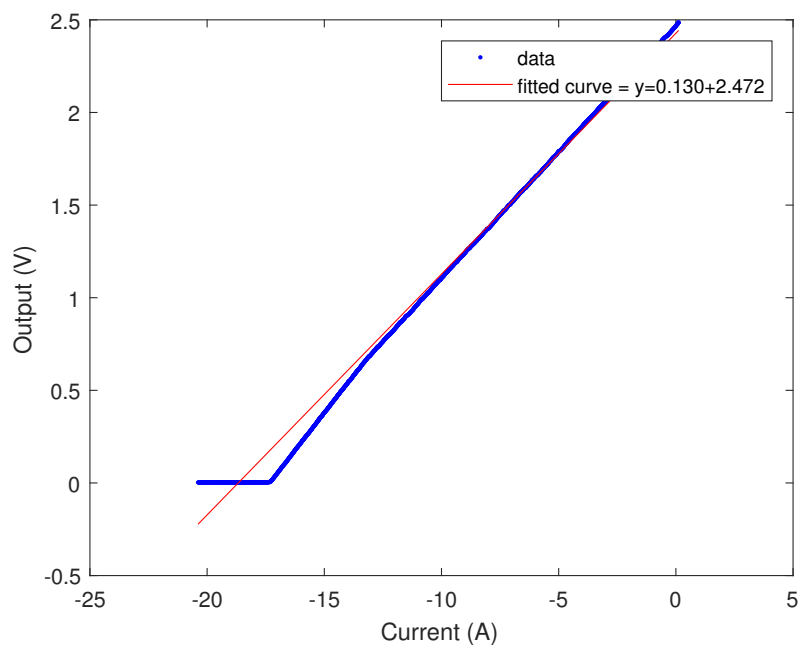
(B) DC test from -20 to 0 A with fitted curve filtered

FIGURE 5.3: DC results

For better understanding of the sensor linearity, the data from 15 to 20 A and -15 to -20 was removed, and the new curve was fitted, thus obtaining for 0 to 15 A range a sensor's sensitivity of $125.8mV/A$ and for 0 to -15 A, a sensibility of $137.4mV/A$. Values were found by fitting the data to a linear equation (Figures 5.4a, 5.4b, 5.5a and 5.5b).
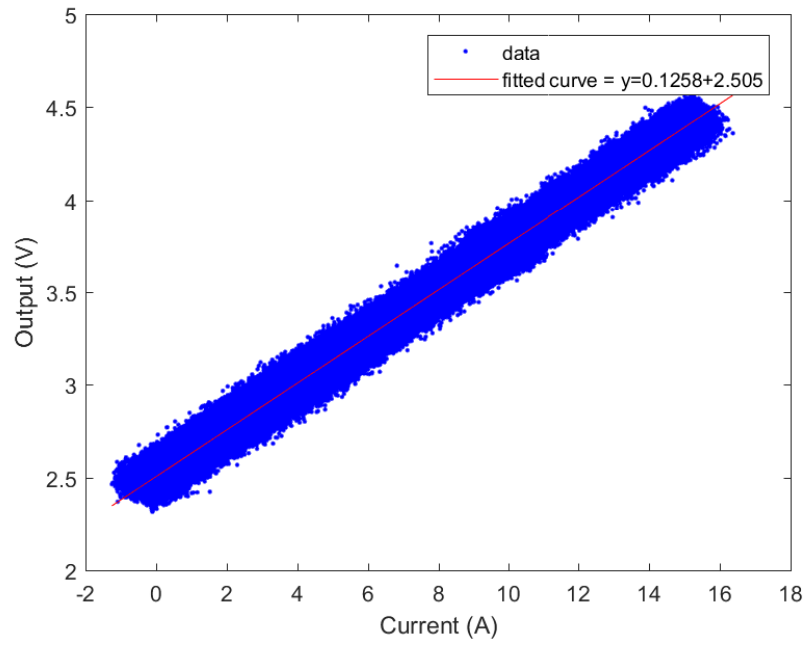
(A) DC test from 0 to 20 with removal of last 5 A and fitted curve
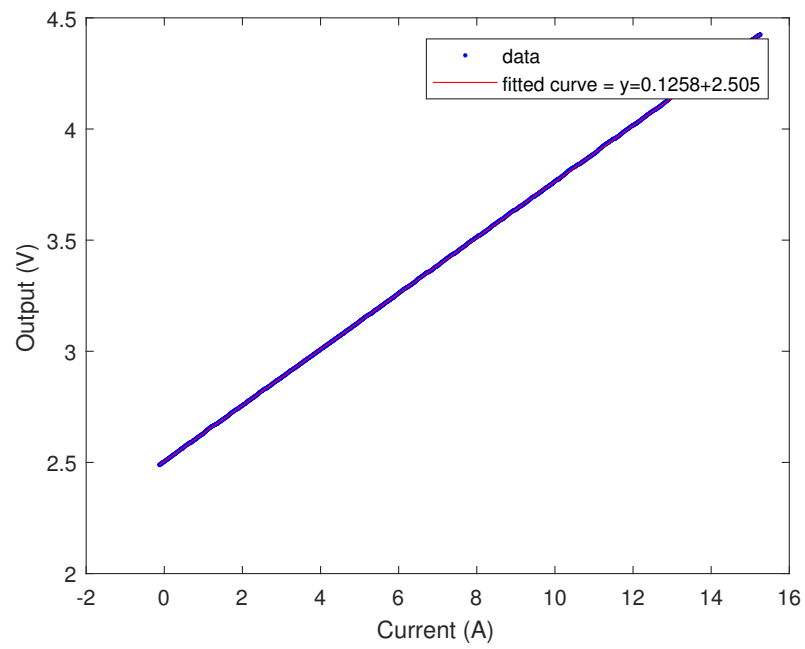
(B) DC test from 0 to 20 A with removal of last 5 A filtered and fitted curve
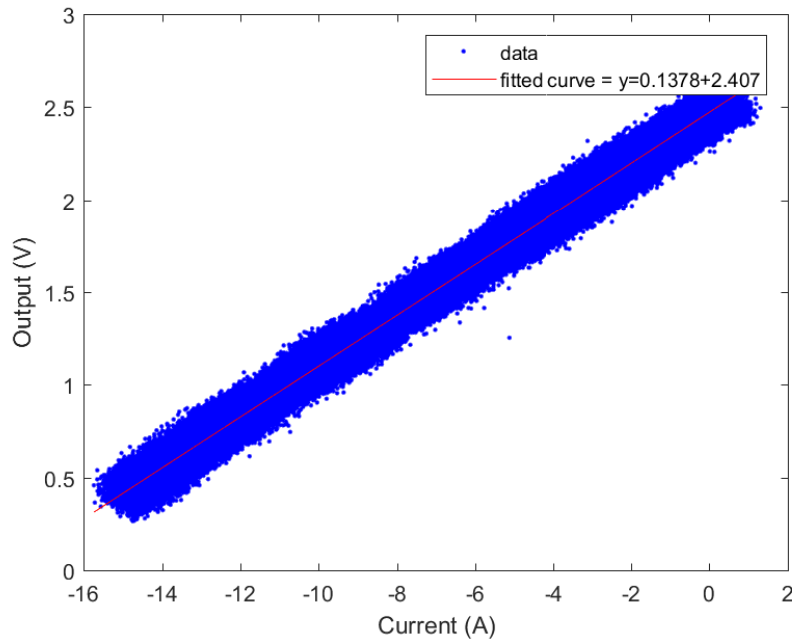
(A) DC test from -20 to 0 A with removal of last 5 A and fitted curve
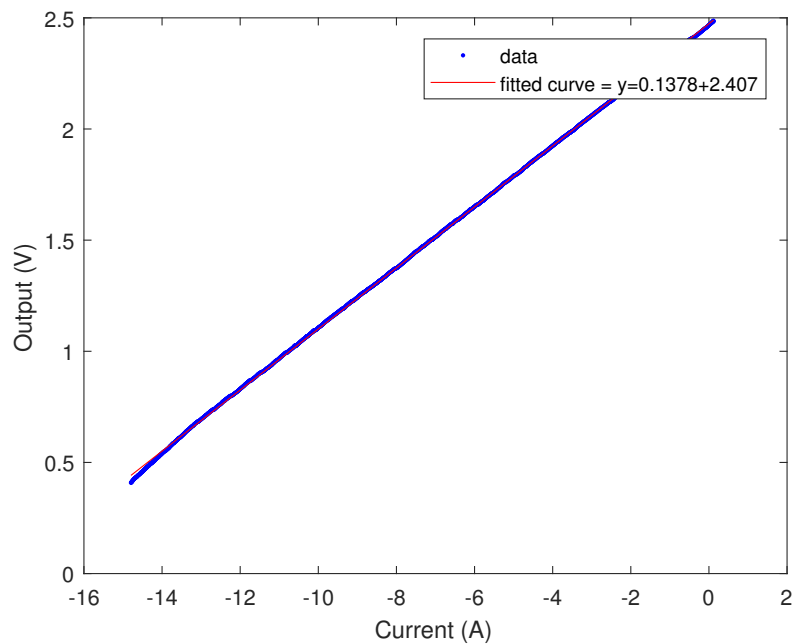
(B) DC test from -20 to 0 A with removal of last 5 A filtered and fitted curve

These errors of sensibility were expected because, as discussed in Chapter 3, the magnetic field at the sensor is not well defined within the simulation, thus leading to gain errors at the adder. To mitigate this problem two potentiometers were added to the design. One for fine tune and the other for a more coarse tune.

Before the beginning of the test, the potentiometers were adjusted until the output of the sensor was equal to Vref. Hereupon, Figures 5.6a and 5.6b represent the new output. Herewith, a sensibility of 99.12 mV/A was obtained, very close the 100mv/A required.

The sensor produces a lot of noise, and one of the possible contributors is these potentiometers, since they are present in the last stage of amplification, the adder. Before the adder, the signals didn't present this magnitude of noise.
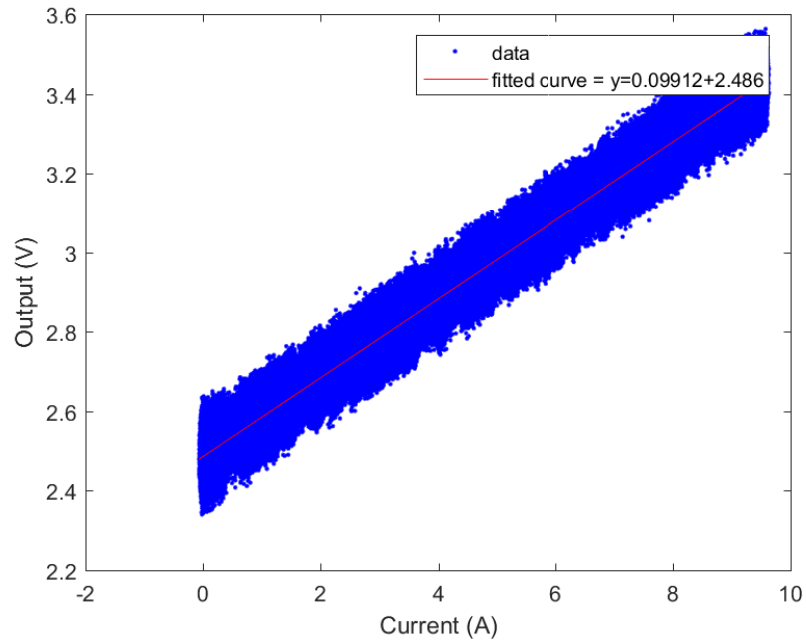
(A) Calibrated sensor output
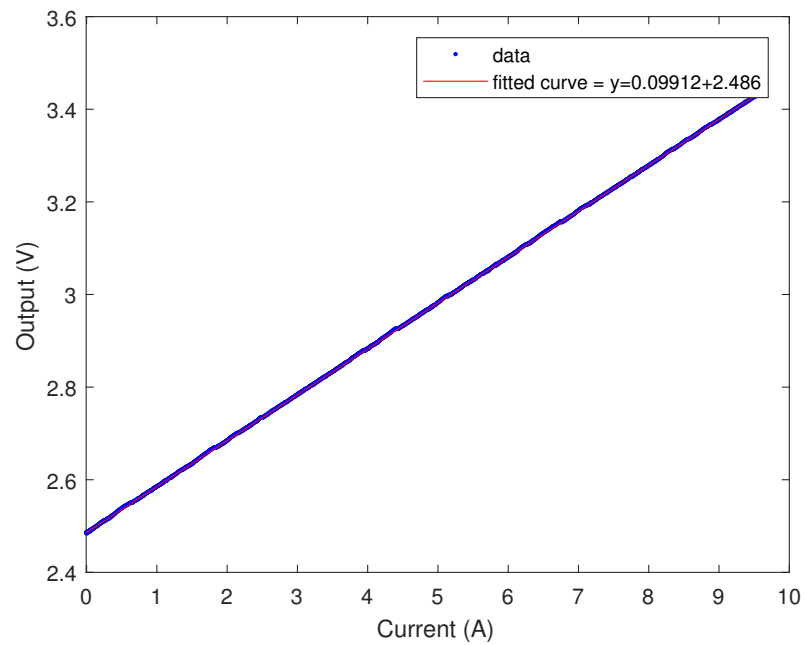
(B) Calibrated sensor output filtered

5.2   AC Test

For this test, the DC component of the sensor was fixed to 2 A, and AC signal was generated. In order to do so, an circuit of current amplification was used. The circuit is illustrated in Figure 5.7
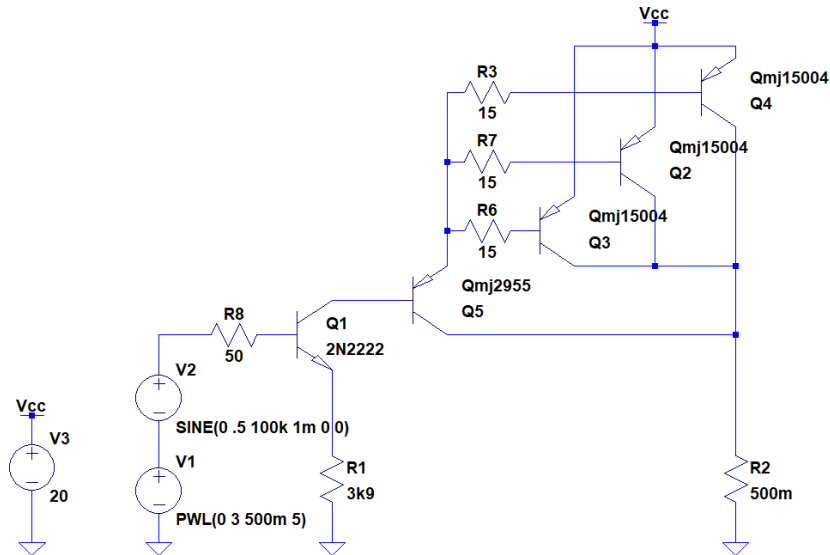
FIGURE 5.7: AC test input current generator

The function of this circuit is basically to amplify an input sine current to a much larger one. This amplified current is now the input current of the test bench. The input of the circuit is a purely sine current, it allows to test the sensor for a range of frequencies and so study it's bandwidth. The input currents had the following frequencies: 1Hz, 10Hz,100Hz, 1 kHz, 10kHz and 100kHz.

Each input current was sensed by the sensor and the reference resistor and for each, the output the Fast Fourier Transform (FFT) was calculated. The following figures represent the output of each sensor for a specific frequency.
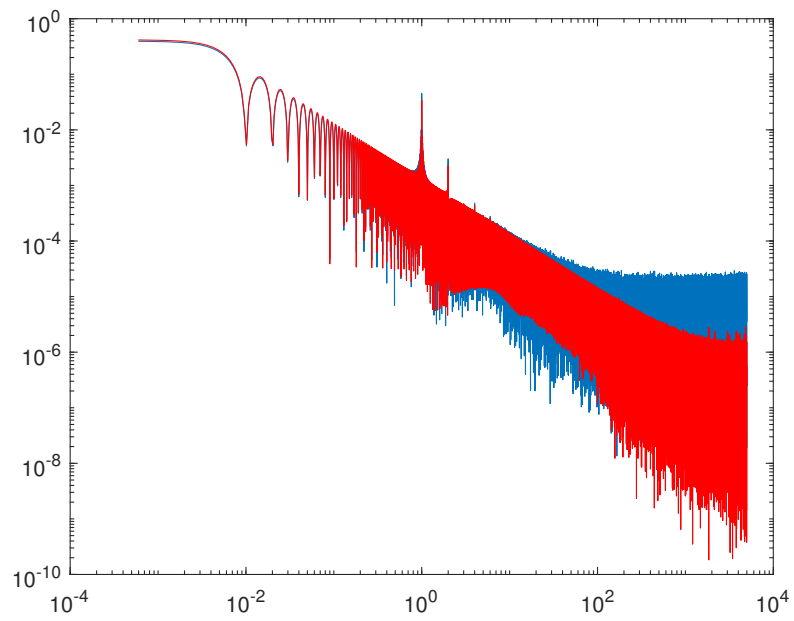
FIGURE 5.8: FFT of the resistor (red line) and sensor (blue line) output for an input signal of 1Hz
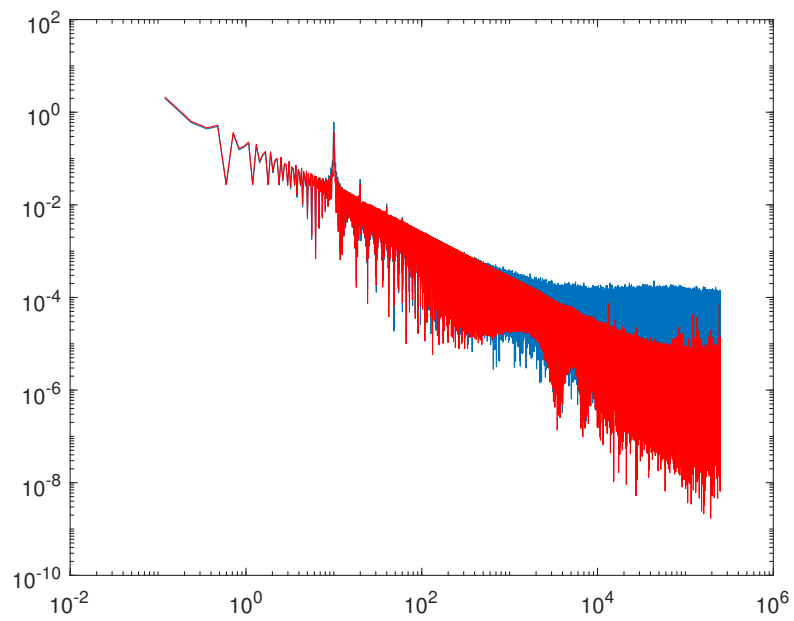
FIGURE 5.9: FFT of the resistor (red line) and sensor (blue line) output for an input signal of 10Hz
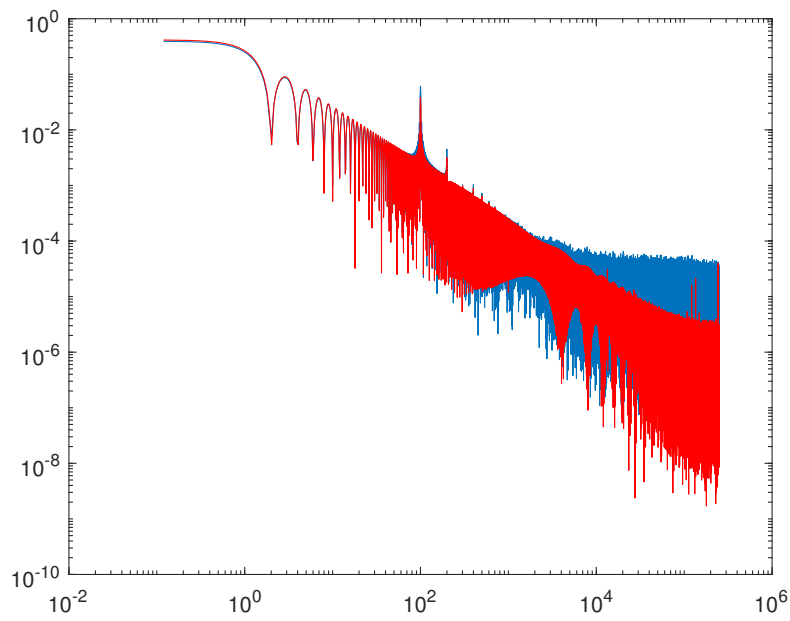
FIGURE 5.10: FFT of the resistor (red line) and sensor (blue line) output for an input signal of 100Hz
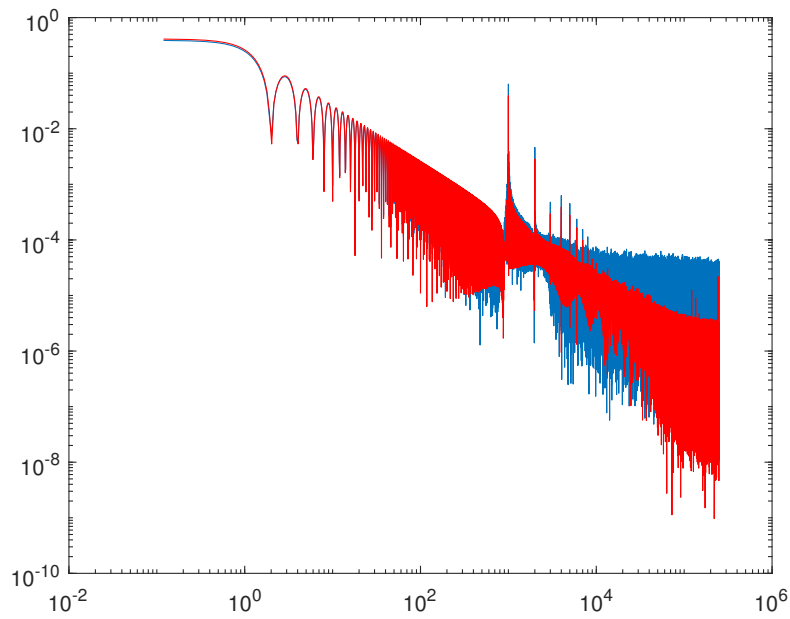
FIGURE 5.11: FFT of the resistor (red line) and sensor (blue line) output for an input signal of 1 kHz
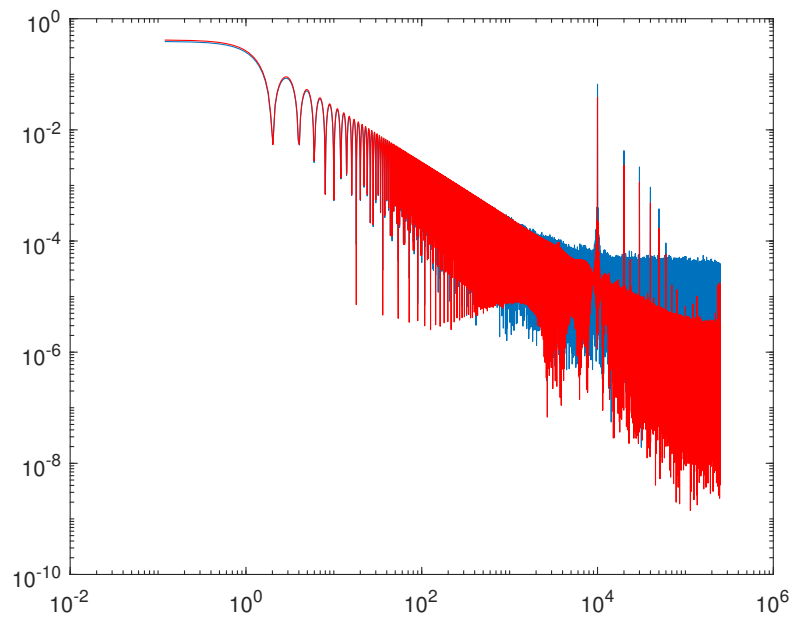
FIGURE 5.12: FFT of the resistor (red line) and sensor (blue line) output for an input signal of 10 kHz
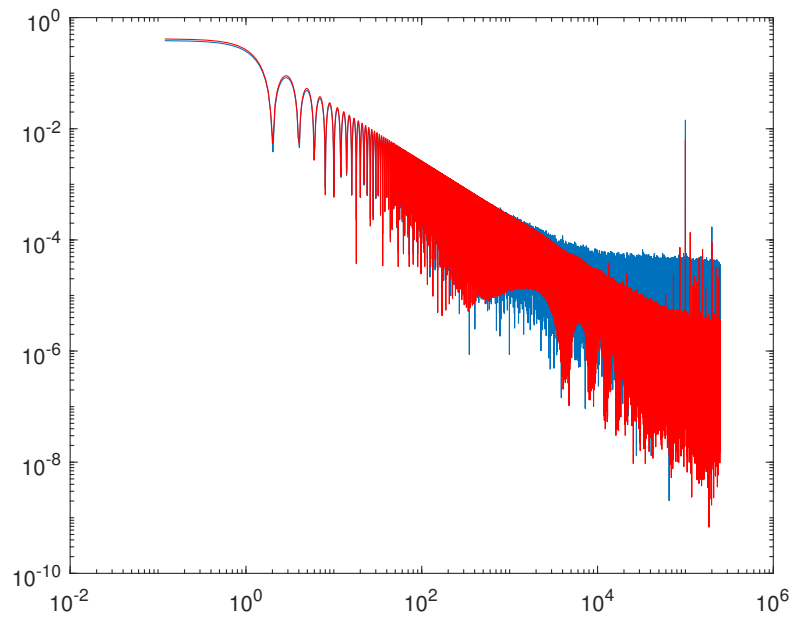
FIGURE 5.13: FFT of the resistor (red line) and sensor (blue line) output for an input signal of 100 kHz

From the figures above it is clear that the amplitudes of the two sensors are not the same, the amplitude of the designed sensor is always higher. One of the possible reasons was that sensor gains, i.e the potentiometers, were not adjusted in the right way.

Table 5.1 exhibits the frequency peaks for each frequency and for each sensor. The ratio of amplitude is also shown in dB.

TABLE 5.1: Results from FFT comparison

Frequency (Hz)	Position (IR)	Amplitude (IR)	Position(IS)	Amplitude (IS)	Ratio (Db)
1	1.01	3.41E-02	1.013	3.46E-02	5.94E-02
10	10.01	3.70E-01	10.01	6.07E-01	2.15E+00
100	100	3.83E-02	100	6.15E-02	2.05E+00
1.00E+03	1000	3.92E-02	1000	6.37E-02	2.10E+00
1.00E+04	1.00E+04	3.86E-02	1.00E+04	6.65E-02	2.36E+00
1.00E+05	1.00E+05	6.23E-03	1.00E+05	1.43E-02	3.59E+00

From Table 5.1, the sensor maintains its performance between 10 Hz and 10 kHz, but for higher frequencies it starts to drop, as expected.

Chapter 6

Conclusion

A current sensor aimed used in space application was designed, built and demonstrated. A proof-of-concept of the design was achieved. The maximum power dissipation obtained was about 350mW, a good value for it's application, thereby contributing to increase the efficiency of Active Spacest PDCU. It also demonstrated good linearity from the range of -15 to 15 A, with the required 100 mV/A sensitivity. The sensor has a good performance between 10 Hz to 10 kHz, however, for low frequencies the sensor must be improved. One of the drawbacks was its noise, around 200mV peak to peak, hindering the measurement of its accuracy and precision. To reduce noise, all the resistors used for gains should be reduced, all the while maintaining the intended gain. For future work the sensors size should be reduced and the copper traces should be thicker to be in conformity with the ECSS.

Besides the work accomplished, this project was a major challenge, forcing me to become a better Physics Engineer. Working alongside engineers who develop instruments for space, was a very worthy and enriching experience and I deeply thank Active Space Technologies for the opportunity of developing my final thesis project with them.

Appendix A

System Requirements and Acceptance Criteria

4.6 Requirements and Acceptance Criteria

Table 4.2 lists the requirements for the system to be developed.

Table 4.2: Requirements list.

ID	Title	Description	Validation
R01	System function	The system shall measure an electrical current.	Demonstration
R02	System modes	The system output shall be a voltage representing the instantaneous electrical current amplitude with four selectable modes: 1) V_{out} = 150 mV/A; V_{offset} = 150 mV 2) V_{out} = 75 mV/A; V_{offset} = 1.65 V 3) V_{out} = 200 mV/A; V_{offset} = 200 mV 4) V_{out} = 100 mV/A; V_{offset} = 2.50 V	Test
R03	Measurement accuracy	The system output shall present an accuracy better than 1% of the reading or 10 mA, whichever is higher.	Test
R04	Measurement precision	The system output shall present a precision better than 2% of the reading or 50 mA, whichever is higher.	Test
R05	Measurement bandwidth	The system output shall present a bandwidth higher than 20 kHz, at -3 dB. The goal is to achieve a bandwidth higher than 100 kHz.	Test
R06	Measurement linearity	The system output shall present a linearity better than 2%.	Test
R07	Electrical current DC component amplitude range	The system shall operate within its nominal specs while measuring an electrical current with DC component in the range of -20 A to 20 A.	Test
R10	Supply voltage	The system shall operate within its nominal specs with a power supply in the voltage range from 3.2 V (TBC) to 5.1 V.	Test
R11	Supply power	The power consumption shall be limited to 100 mW.	Test
R12	Aerospace application	The system design shall seek to employ components qualified for space applications or components identified as equivalent to qualified components.	Review
R13	System mass	The system design shall seek mass minimization.	Review
R14	System volume	The system design shall seek volume minimization.	Review
R15	Operating temperature	The system shall operate within its nominal specs with an ambient temperature range from -20 °C to 50 °C.	Test
R16	System integration	The system shall be reasonably easy to integrate in the by the end user, namely not requiring excessive placement precision or time consuming procedures.	Inspection

Appendix B

Electrical schematic of sensor

Transducer1
Transducer1.SchDoc
- VDRIVER1_OFFSET-
- VDRIVER1_OFFSET+
- SENSOR1_OUT+
- SENSOR1_OUT-
- SR_OUT

Transducer2
Transducer2.SchDoc
- SENSOR2_OUT+
- SENSOR2_OUT-
- VDRIVER2_OFFSET-
- VDRIVER2_OFFSET+
- SR_OUT

Diff
Dif_Amplifier.SchDoc
- SENSOR1_OUT+
- SENSOR1_OUT-
- SENSOR2_OUT+
- SENSOR2_OUT-
- VSENSE1_AC
- VSENSE2_AC

Filter
Filter.SchDoc
- VSENSE1_AC
- VSENSE2_AC
- VFILTER1_OUT
- VFILTER2_OUT

Driver
Driver.SchDoc
- VFILTER1_OUT
- VFILTER2_OUT
- VDRIVER1_OFFSET+
- VDRIVER1_OFFSET-
- VDRIVER2_OFFSET-
- VDRIVER2_OFFSET+

Adder
Adder.SchDoc
- VDRIVER1_OFFSET+
- VSENSE1_AC
- VSENSE2_AC
- VDRIVER2_OFFSET+
- OUT

Power
Power.SchDoc

SetReset
SetReset.SchDoc
- SR_IN
- SR_OUT

bom
AST_A4_No_BOM_Parts.SchDoc

VCC
C12 1uF
C13 10uF
C14 220uF
GND

H3 SYSTEM_OUT
H5 SYSTEM_OUT
H4 1 2 Jumper
H6 SYSTEM_OUT
H7 SYSTEM_OUT
H8 SYSTEM_OUT
H9 SYSTEM_OUT
H10 SYSTEM_OU
H11 SYSTEM_OUT
H14 SYSTEM_OUT
H12 SYSTEM_OUT
H15 SYSTEM_OUT
H13 SYSTEM_OUT
H16 SYSTEM_OUT
H19 SR_IN

MeasCurr
H17 CURRENT
CURRENT
H18 CURRENT
CURRENT

[BAntunes, 2017-06-06 14:46]
1) Define correctly the direction of every sheet entry.
2) The system was supposed to have an output... I could not find it.
3) How do you interface with this board? No headers, no connectors... Is it wireless technology? Does it harvest its own power? :)
4) Reorganize. Go for a scheme in which info/data/power/signals/whatever preferably travel from left to right and from top to down. I would suggest to make this sheet look like the first drawing of the PDF I've sent to you on May 19.

activespace technologies

ISSUE	DESCRIPTION	DATE	DESIGNER

APPROVALS	INITIALS	SIGNATURES	DATE
DRAWN BY	<5>		<6>
CHECKED BY	<7>		<8>
APPROVED BY	<13>		<14>

TITLE <a>
SIZE A4
HW REFERENCE <1>
HW SHORT REFERENCE <2>
SHEET 1 of 10
SCHEMATIC FILE NAME Top_Sheet.SchDoc
HW VARIANT NoVariant
ISSUE <4>

1 2 3 4

A B C D

VCC

SENSOR1_OUT+

U11
1	OUT+	OFFSET-	8
2	VBRIDGE	OFFSET+	7
3	GND	S/R-	6
4	OUT-	S/R+	5

HMC1021S

SENSOR1_OUT-

VDRIVER1_OFFSET-
VDRIVER1_OFFSET+

SR_OUT

GND

GND

VCC
C31 1uF   C32 100nF
GND

1 Net Class

[BAntunes, 2017-06-06 15:09]
1) Avoid superposed objects;
2) Change Vref symbol. The one taken is used for signal ground (typically digital).
3) Preferably, use ALL_CAPS for ports and net labels. This is only a "good practice", just like identation in SW code, but may help you avoid future errors/problems, namely during the layout stage.
4) I would split this sheet into multiple sheets. there are a few advantages. Readability, for starters. But, most importantly, when you get to transfer the schematics to the PCB layout, components will appear grouped in "rooms". Rooms are very good. Designers like rooms very much. You will be interested in having each room with a relatively small number of components that MUST BE PLACED CLOSELY TOGETHER. As an example, if you transfer the shematics to the PCB as they are, you will most likely end up with capacitors C21, C22, C23, C24, C25, C26, C27, C28, C29, C30, C31, C32, C33, and C34 all together in a corner, thus loosing info of their purpose and related chip without coming back to the schematics for cross checking.
5) Define correctly the direction of every non-power port.

ISSUE	DESCRIPTION	DATE	DESIGNER

APPROVALS	INITIALS	SIGNATURES	DATE
DRAWN BY	<5>		<6>
CHECKED BY	<7>		<8>
APPROVED BY	<13>		<14>

TITLE <a>   SIZE A4

HW REFERENCE <1>   HW SHORT REFERENCE <2>   SHEET 2 of 10

SCHEMATIC FILE NAME Transducer1.SchDoc   HW VARIANT NoVariant   ISSUE <4>

activespace technologies

VCC

SENSOR2_OUT+

U12

1	OUT+	OFFSET-	8
2	VBRIDGE	OFFSET+	7
3	GND	S/R-	6
4	OUT-	S/R+	5

HMC1021S

GND

SENSOR2_OUT-

VDRIVER2_OFFSET-

VDRIVER2_OFFSET+

SR_OUT

GND

VCC

C33 1uF   C34 100nF

GND

i Net Class

Transducer

ISSUE	DESCRIPTION	DATE	DESIGNER

APPROVALS	INITIALS	SIGNATURES	DATE	TITLE <a>		SIZE A4
DRAWN BY	<5>		<6>	HW REFERENCE <1>	HW SHORT REFERENCE <2>	SHEET 3 of 10
CHECKED BY	<7>		<8>			
APPROVED BY	<13>		<14>	SCHEMATIC FILE NAME Transducer2.SchDoc	HW VARIANT NoVariant	ISSUE <4>

VCC

C15 C16
1uF 100nF

GND

VCC

U6
INA149-EP

7

SENSOR1_OUT- 2
SENSOR1_OUT+ 3
INA149 6 VSENSE1_AC
5 1
4

VREF

GND

VCC

U7
INA149-EP

7

SENSOR2_OUT- 2
SENSOR2_OUT+ 3
INA149 6 VSENSE2_AC
5
4

VREF

GND

VCC

C17 C18
1uF 100nF

GND

i
Net Class

[BAntunes, 2017-06-06 15:09]
1) Avoid superposed objects;
2) Change Vref symbol. The one taken is used for signal ground (typically digital).
3) Preferably, use ALL_CAPS for ports and net labels. This is only a "good practice", just like identation in SW code, but may help you avoid future errors/problems, namely during the layout stage.
4) I would split this sheet into multiple sheets. there are a few advantages. Readability, for starters. But, most importantly, when you get to transfer the schematics to the PCB layout, components will appear grouped in "rooms". Rooms are very good. Designers like rooms very much. You will be interested in having each room with a relatively small number of components that MUST BE PLACED CLOSELY TOGETHER. As an example, if you transfer the schematics to the PCB as they are, you will most likely end up with capacitors C21, C22, C23, C24, C25, C26, C27, C28, C29, C30, C31, C32, C33, and C34 all together in a corner, thus loosing info of their purpose and related chip without coming back to the schematics for cross checking.
5) Define correctly the direction of every non-power port.
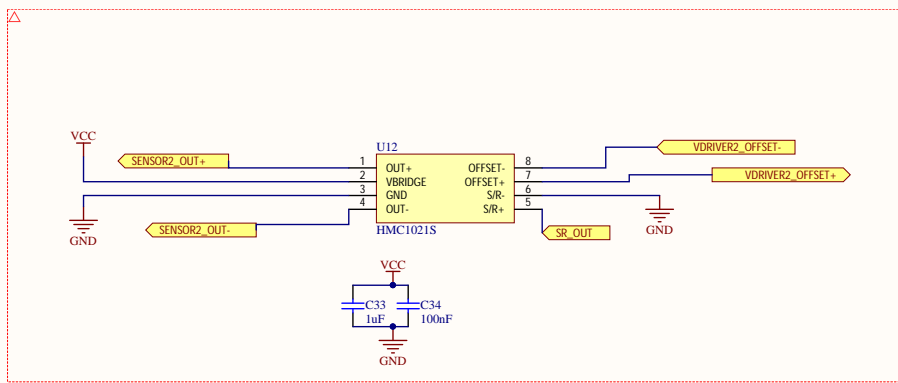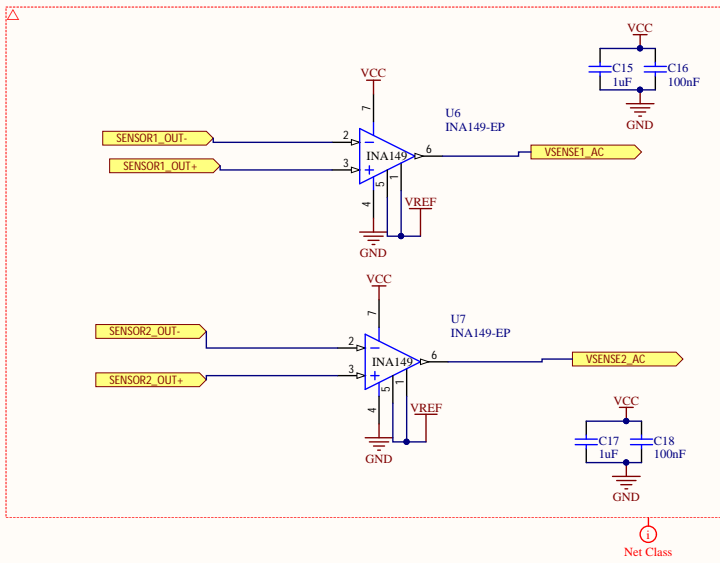
ISSUE	DESCRIPTION	DATE	DESIGNER

activespace
technologies

APPROVALS	INITIALS	SIGNATURES	DATE			
DRAWN BY	<5>		<6>	TITLE <a>		SIZE A4
CHECKED BY	<7>		<8>	HW REFERENCE <1>	HW SHORT REFERENCE <2>	SHEET 4 of 10
APPROVED BY	<13>		<14>	SCHEMATIC FILE NAME Dif_Amplifier.SchDoc	HW VARIANT NoVariant	ISSUE <4>

Filter

C25
1uF

VFILTER1_OUT

VCC

VFILTER2_OUT

VSENSE1_AC

R19
33K

R20
33K

C27
1uF

GND

R21
1K

U10
1 OUT_A   V+ 8
2 -IN_A   OUT_B 7
3 +IN_A   -IN_B 6
4 V-   +IN_B 5
AD8629-EP

R22
1K

C26
1uF

R23
33K

R24
33K

VSENSE2_AC

C28
1uF

GND

GND

VCC

C29
1uF

C30
100nF

GND

Net Class

Driver

VREF

R11
4k02

C19
470n

R13
76K8

R14
3K3

VCC

U8
OPA365-EP

5

4

3

2

1

A

V+
V-

GND

VFILTER1_OUT

PID errado

VREF

R12
1R

VDRIVER1_OFFSET+

VDRIVER1_OFFSET-

VCC

C20
1uF

C21
100nF

GND

VREF

R15
4k02

C22
470n

R17
76K8

R18
3K3

VCC

U9
OPA365-EP

5

4

3

2

1

A

V+
V-

GND

VFILTER2_OUT

PID errado

VREF

R16
1R

VDRIVER2_OFFSET+

VDRIVER2_OFFSET-

VCC

C23
1uF

C24
100nF

GND

Net Class

[BAntunes, 2017-06-06 15:09]
1) Avoid superposed objects;
2) Change Vref symbol. The one taken is used for signal ground (typically digital).
3) Preferably, use ALL_CAPS for ports and net labels. This is only a "good practice", just like identation in SW code, but may help you avoid future errors/problems, namely during the layout stage.
4) I would split this sheet into multiple sheets. there are a few advantages. Readability, for starters. But, most importantly, when you get to transfer the schematics to the PCB layout, components will appear grouped in "rooms". Rooms are very good. Designers like rooms very much. You will be interested in having each room with a relatively small number of components that MUST BE PLACED CLOSELY TOGETHER. As an example, if you transfer the shematics to the PCB as they are, you will most likely end up with capacitors C21, C22, C23, C24, C25, C26, C27, C28, C29, C30, C31, C32, C33, and C34 all together in a corner, thus loosing info of their purpose and related chip without coming back to the schematics for cross checking.
5) Define correctly the direction of every non-power port.

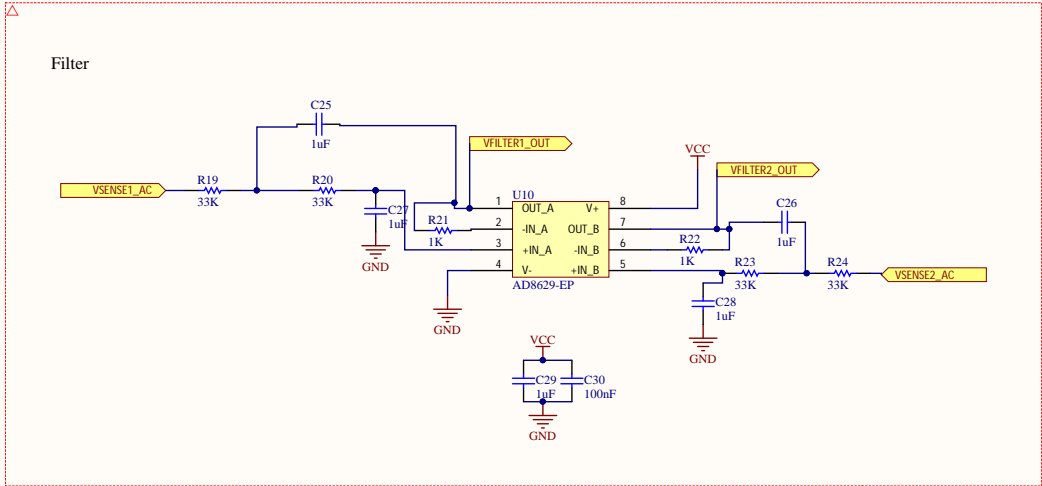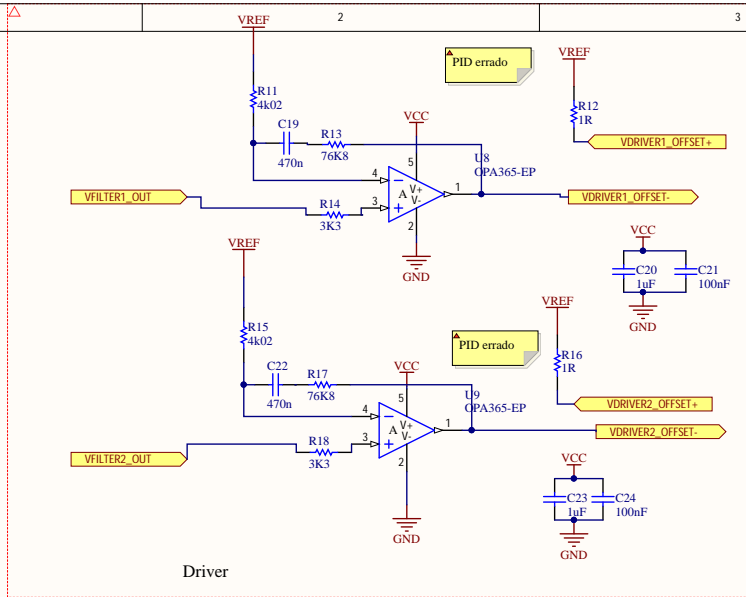| ISSUE	DESCRIPTION	DATE	DESIGNER

activespace
technologies

APPROVALS	INITIALS	SIGNATURES	DATE	TITLE		SIZE
DRAWN BY	<5>		<6>	<a>		A4
CHECKED BY	<7>		<8>	HW REFERENCE <1>	HW SHORT REFERENCE <2>	SHEET 6 of 10
APPROVED BY	<13>		<14>	SCHEMATIC FILE NAME Driver.SchDoc	HW VARIANT NoVariant	ISSUE <4>

Ganho errado, calcular com valores reais
calcular potenciometro

VSENSE1_AC
VDRIVER1_OFFSET+
VSENSE2_AC
VDRIVER2_OFFSET+

VCC
C1 1uF   C2 100nF
GND

VCC
VREF
U1 INA149-EP
VREF
GND

VCC
VREF
U3 INA149-EP
VREF
VCC
C5 1uF   C6 100nF
GND
GND

R1 3kΩ
R2 3kΩ
R3 100K   50k   1k

VREF
VCC
U2 OPA365-EP
GND
OUT

R4 1K84
R5 1K84
R6 2K
R7 2K

VCC
C3 1uF   C4 100nF
GND

Net Class
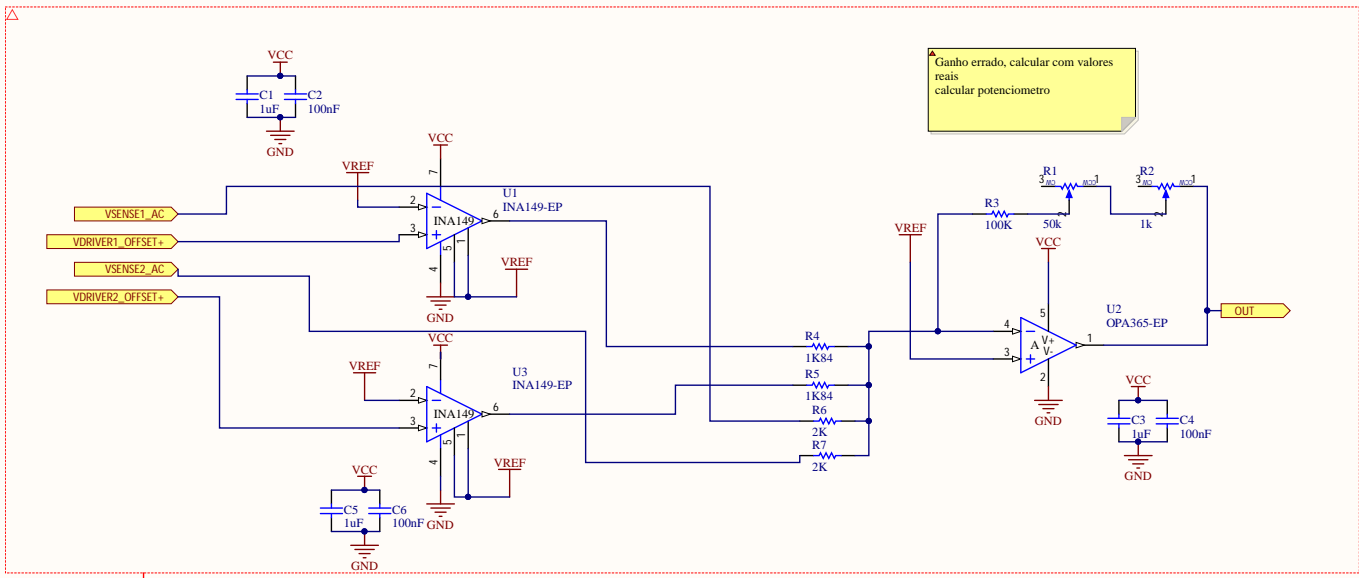
[BAntunes, 2017-06-06 14:28]
1) Avoid superposed objects;
2) Change Vref symbol. The one taken is used for signal ground (typically digital).
3) Preferably, use ALL_CAPS for ports and net labels. This is only a "good practice", just like identation in SW code, but may help you avoid future errors/problems, namely during the layout stage.
4) All the four non-power ports in this sheet are supposed to be inputs, instead of bidirectional.
5) At least an output port is missing in this sheet.
6) There is a capacitor lost somewhere in this sheet. Do you feel like finding it on your own? Come to me if you cannot ;)
7) Device U2 has its pin 1 short circuited to GND!!! Furthermore, such fact is identified as an error... Dude... That is, most likely, the source for the remaining 3 errors identified in this sheet.

activespace
technologies

ISSUE	DESCRIPTION	DATE	DESIGNER

APPROVALS	INITIALS	SIGNATURES	DATE
DRAWN BY	<5>		<6>
CHECKED BY	<7>		<8>
APPROVED BY	<13>		<14>

TITLE <a>   SIZE A4
HW REFERENCE <1>   HW SHORT REFERENCE <2>   SHEET 7 of 10
SCHEMATIC FILE NAME Adder.SchDoc   HW VARIANT NoVariant   ISSUE <4>

VCC

C7
1uF

C8
100nF

GND

D1

2

R8
2K49

1

VCC

VCC

3

U5
OPA365-EP

VREF

H1

GND

5

4

−
A V+
V−
+

1

TEST_VREF

LT1009

3

3

2

GND

GND

Net Class

[BAntunes, 2017-06-06 14:07]
1) Avoid superposed objects;
2) You state there's a missing potentiometer. Explain & place it.
3) Change Vref symbol. The one taken is used for signal ground (typically digital).
4) Preferably, use ALL_CAPS for ports and net labels. This is only a "good practice", just like identation in SW code, but may help you avoid future errors/problems, namely during the layout stage.

ISSUE	DESCRIPTION	DATE	DESIGNER

activespace
technologies

APPROVALS	INITIALS	SIGNATURES	DATE	TITLE <a>		SIZE A4
DRAWN BY	<5>		<6>	HW REFERENCE <1>	HW SHORT REFERENCE <2>	SHEET 8 of 10
CHECKED BY	<7>		<8>			
APPROVED BY	<13>		<14>	SCHEMATIC FILE NAME Power.SchDoc	HW VARIANT NoVariant	ISSUE <4>

VCC

R10
232R

C11
2.2uF

GND

Q1B
IRF7389

4

3

R9
1K

SR_IN

C10
100nF

C9
100nF

SR_OUT

H2
TEST_SR

Q1A
IRF7389

2

Net Class

Net Class

GND

[BConceição, 2017-06-06 16:07]

Space qualified transistores must be picked

[BAntunes, 2017-06-06 15:35]
1) Avoid superposed objects;
2) Is not SR_IN an input port?
3) SR1+ and SR2+ are two ports that provide output of the very same net. This is not a good design. Effect: a warning says that net has two names...
4) Reorganize. Go for a scheme in which info/data/power/signals/whatever preferably travel from left to right and from top to down.
5) I understand this is not finished.

ISSUE	DESCRIPTION	DATE	DESIGNER

activespace
technologies

APPROVALS	INITIALS	SIGNATURES	DATE
DRAWN BY	<5>		<6>
CHECKED BY	<7>		<8>
APPROVED BY	<13>		<14>

TITLE
<a>

SIZE
A4

HW REFERENCE
<1>

HW SHORT REFERENCE
<2>

SHEET
9 of 10

SCHEMATIC FILE NAME
SetReset.SchDoc

HW VARIANT
NoVariant

ISSUE
<4>

I1
AST Logo, Top Layer, No Motto

I2
_HW_Reference
ISSUE <4>
AST Reference & Issue, Cooper Layers

I3
AST Logo, Top Overlay, No Motto

I4
_HW_Reference
ISSUE <4>
AST Reference & Issue, Overlay

FD1
Fiducial in cooper Top and Bottom Layer

FD2
Fiducial in cooper Top and Bottom Layer

SC1
Screw M3x5 SHCS

SC2
Screw M3x5 SHCS

SC3
Screw M3x5 SHCS

SC4
Screw M3x5 SHCS

APPROVALS	INITIALS	SIGNATURES	DATE	TITLE		SIZE
DRAWN BY	<5>		<6>	<a>		A4
CHECKED BY	<7>		<8>	HW REFERENCE <1>	HW SHORT REFERENCE <2>	SHEET 10 of 10
APPROVED BY	<13>		<14>	SCHEMATIC FILE NAME AST_A4_No_BOM_Parts.SchDoc	HW VARIANT NoVariant	ISSUE <4>

Appendix C

Bill of materials of sensor

#	Designator	Part Number	Quantity	replaced with	ordered Mouser PO-0062	ordered Digikey PO-0063	Description	Footprint
1	C1, C3, C5, C7, C12, C20, C23, C25, C26, C27, C28, C29	GRM188R61E105KA12D	12	CGA3E1X7R1V105K080AC	500		MLCC, 0603, 25V, X5R, 1uF	cap1608/0603
2	C2, C4, C6, C8, C21, C24, C30 (check line 3)	MCCA000160	7	06035C104KAT2A	500		MLCC, 0603, Y5V, 16V,100nF	cap1608/0603
3	C9, C10	MC0603B104K500CT	2	same as previous line...	-		MLCC, 0603, X7R, 50V, 100nF	cap1608/0603
4	C11	C1608X5R1V225K	1	EMK107BJ225MA-T	10		MLCC, 0603, 35V, X5R, 2.2uF	cap1608/0603
5	C13	C1608X5R1E106M	1	GRM188R61E106MA73D	10		MLCC, 0603, 25V, X5R, 10uF	cap1608/0603
6	C14	GRM31CR60J227ME11L	1	F951A107KAAAQ2		10	MLCC, 0603, X5R, 6,3V, 220uF	cap3216/1206
7	C15, C17, C31, C33	B37941K0105K62	4	08053C105KAT4A	15		MLCC, 0805, X7R, 25V, 1uF	cap2012/0805
8	C16, C18, C32, C34	U0805F104ZCT	4	885012207072	15		MLCC, 0805, Y5V, 50V, 0.1µF	cap2012/0805
9	C19, C22	C1608X5R1H474K080AB	2	UMK107ABJ474KA-T	15		MLCC, 0603, 50V X5R, 470nF	cap1608/0603
10	D1	LT1009CLPR	1		5		2.5-V INTEGRATED REFERENCE CIRCUIT	TO-92-3_Straight_Leads
11	Q1	IRF7389TRPBF	1		5		Dual N+P-Channel MOSFET	SO8
12	R1	PVG5A503C03R00	1		2		Trimpot, 11 turns, 50K	PVG5A
13	R2	PVG5A102C03R00	1		2		Trimpot, 11 turns, 1K	PVG5A
14	R3	ERJ-3EKF1003V	1	RC0603FR-07100KL	100		RESISTOR, 0603, 100K, 1%	res1608/0603
15	R4, R5	603-RT0603BRD071K84L	2	(not replaced, but this is a 0.1% tolerance resistor)	10		RESISTOR, 0603, 1K84, 1%	res1608/0603
16	R6, R7	ERJ-3EKF2001V	2	APC0603B2K00N (0.1% tolerance)	10		RESISTOR, 0603, 2K, 1%	res1608/0603

#	Designator	Part Number	Qty	Alt Part Number			Description	Package
17	R8	RP73PF1J2K49BTDF	1	CPF0603B2K49E1	5		RESISTOR, 0603, 2.49K, 0.1%, 25ppm/°C	res1608/0603
18	R9	CRCW06031K00FKEA	1	RC0603FR-071KL	100		RESISTOR, 0603, 1K, 1%	res1608/0603
19	R10 (check line 25)	CRCW0603232RFKEA	1		100		RESISTOR, 0603, 232R, 1%	res1608/0603
20	R11, R15	ERJ-1GEF4021C	2	CRCW06034K02FKEA	100		RESISTOR, 0603, 4K02, 1%	res1608/0603
21	R12, R16	ERJ-1GEJ1R0C	2	RT0603DRE071RL	10		RESISTOR, 0603, 1R, 5%	res1608/0603
22	R13, R17	ERA-3AEB7682V	2	CRCW060376K8FKEA	100		RESISTOR, 0603, 76K8, 1%	res1608/0603
23	R14, R18	ERJ-3EKF3301V	2	RC0603FR-073K3L	100		RESISTOR, 0603, 3.3K , 1%	res1608/0603
24	R19, R20, R23, R24	ERJ-3EKF3302V	4	RC0603FR-0733KL	100		RESISTOR, 0603, 33K, 1%	res1608/0603
25	R21, R22	ERJ-3EKF1001V	2	(use line 19: RC0603FR-071KL)	-		RESISTOR, 0603, 1K , 1%	res1608/0603
26	U1, U3, U6, U7	INA149AMDREP	4	INA149AIDR	6	3	High Common Mode Voltage Difference Amplifier ENHanced product	SOIC-8
27	U2, U5, U8, U9	OPA365AMDBVTEP	4	OPA365AIDR	6	3	Operational Amplifier, rail-to-rail, single supply	SOT23-5
28	U10	AD8629ARZ	1		3		Operational Amplifier, Dual, 2 Amplifier, 2.5 MHz, 1 V/µs, 2.7V to 5V,	SOIC-8
29	U11, U12	HMC1021S	2			5	Magnetoresistive sensor	SOIC-8

Appendix D

PCB layout of sensor
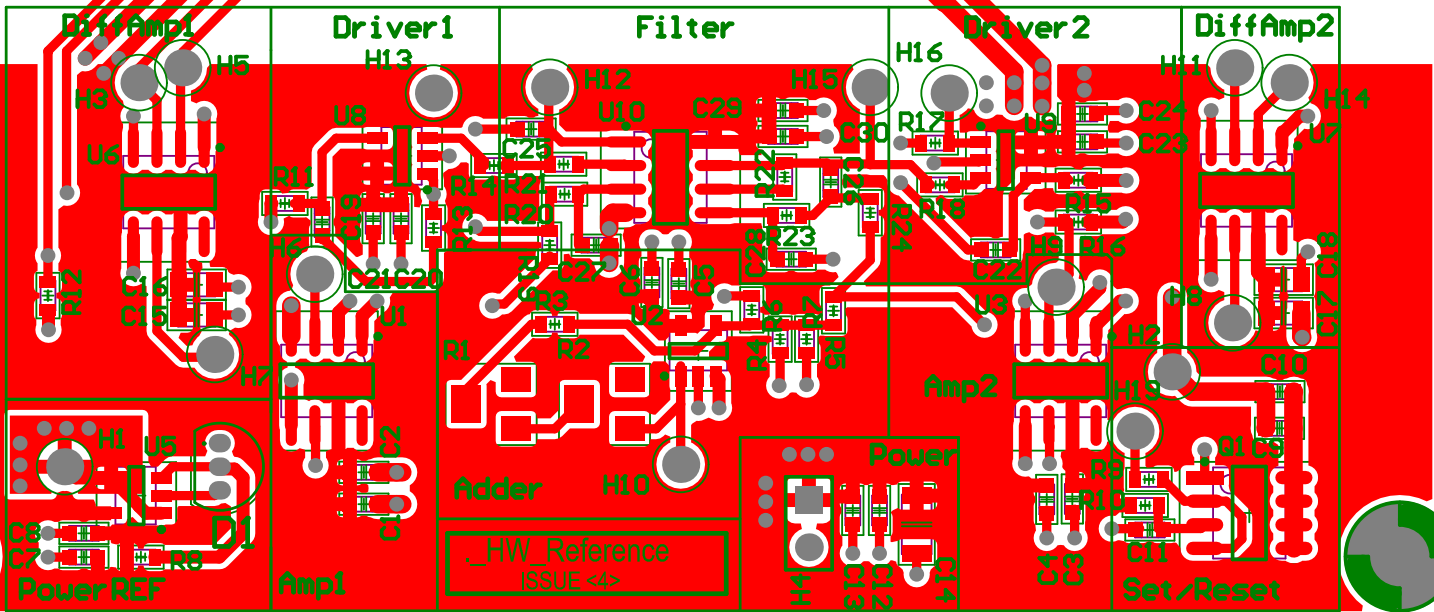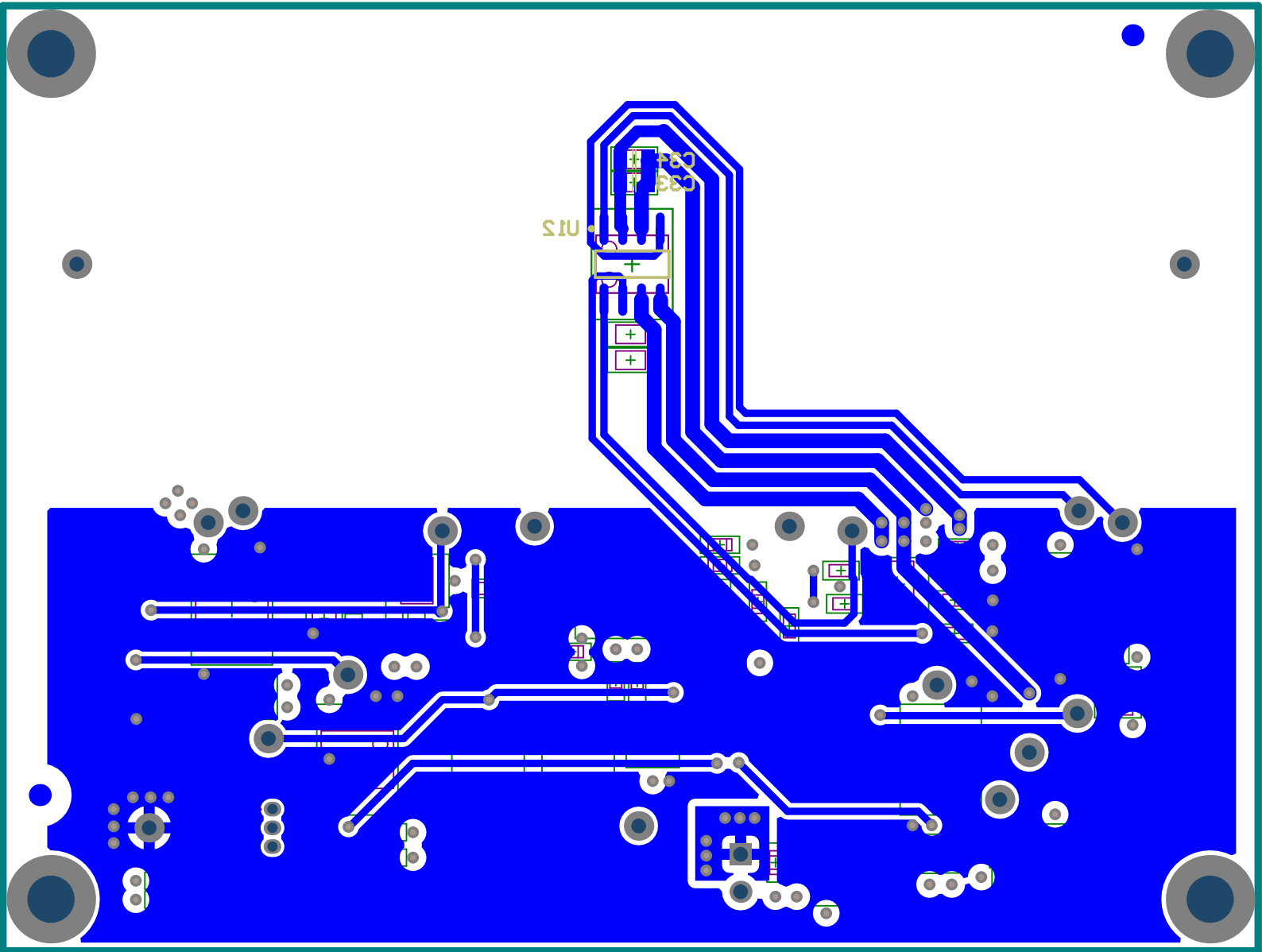
Bibliography

[1]   Miria M. Finckenor and Kim K. de Groh. "Space Environmental Effects". In: (2015), p. 40. URL: `https://www.nasa.gov/sites/default/files/files/NP-2015-03-015-JSC{\_}Space{\_}Environment-ISS-Mini-Book-2015-508.pdf`.

[2]   *Earth's Atmosphere - Reference Library - RedOrbit. [Online].* `http://www.redorbit.com/education/reference_library/atmosphere/earths_atmosphere/352/index.html/`.

[3]   V Lakshminarayana et al. "Impact of Space weather on Spacecraft". In: (), pp. 1–6.

[4]   Daniel M. Fleetwood, Peter S. Winokur, and Paul E. Dodd. "An overview of radiation effects on electronics in the space telecommunications environment". In: *Microelectronics Reliability* 40 (2000), pp. 17–26. ISSN: 00262714. DOI: `10.1016/S0026-2714(99)00225-5`. URL: `http://www.sciencedirect.com/science/article/pii/S0026271499002255`.

[5]   T. Asada, W.G. Odendaal, and J.D. van Wyk. "An overview of integratable current sensor technologies". In: *38th IAS Annual Meeting on Conference Record of the Industry Applications Conference, 2003.* 2 (2003), pp. 1251–1258. ISSN: 01972618. DOI: `10.1109/IAS.2003.1257710`. URL: `http://ieeexplore.ieee.org/lpdocs/epic03/wrapper.htm?arnumber=1257710`.

[6]   Silvio Ziegler et al. "Current Sensing Techniques: A Review". In: *IEEE Sensors Journal* 9.4 (2009), pp. 354–376. ISSN: 1530-437X. DOI: `10.1109/JSEN.2009.2013914`. URL: `http://ieeexplore.ieee.org/lpdocs/epic03/wrapper.htm?arnumber=4797906`.

[7]   James E. Lenz. "A Review of Magnetic Sensors". In: *Proceedings of the IEEE* 78.6 (1990), pp. 973–989. ISSN: 15582256. DOI: `10.1109/5.56910`.

[8]   Marina Díaz-Michelena. "Small magnetic sensors for space applications". In: *Sensors* 9.4 (2009), pp. 2271–2288. ISSN: 14248220. DOI: `10.3390/s90402271`.

[9]   LEM. *Industry Current & Voltage Transducers.* `https://www.iconopower.com/v/lem/Industry&20Current&20Voltage&20Transducers.pdf`. original document from LEM. 2011.

[10] Albrecht Jander, Carl Smith, and Robert Schneider. "Magnetoresistive sensors for nondestructive evaluation". In: *Proceedings of SPIE* (2005), pp. 1–13. ISSN: 0277786X. DOI: `10.1117/12.601826`. URL: `http://link.aip.org/link/?PSI/5770/1/1{\&}Agg=doi{\%}5Cnhttp://proceedings.spiedigitallibrary.org/proceeding.aspx?articleid=1325845`.

[11]   Tin Yan Poon, Norman Chung Fai Tse, and Ricky Wing Hong Lau. "Extending the GMR current measurement range with a counteracting magnetic field". In: *Sensors (Switzerland)* 13.6 (2013), pp. 8042–8059. ISSN: 14248220. DOI: 10.3390/s130608042.

[12]   M D. Michelena. "Commercial Off-The-Shelf GMR Based Sensor on Board Optos Picosatellite". In: 6 (Jan. 2013), pp. 181–210.

[13]   M. D. Michelena et al. "COTS-based wireless magnetic sensor for small satellites". In: *IEEE Transactions on Aerospace and Electronic Systems* 46.2 (2010), pp. 542–557. ISSN: 00189251. DOI: 10.1109/TAES.2010.5461640.

[14]   honeywell. *1- and 2-Axis Magnetic Sensors HMC1001/1002/1021/1022*. https://neurophysics.ucsd.edu/Manuals/Honeywell/HMC%201001%20and%20HMC%201002.pdf. Datasheet HMC1001/1002/1021/1022.

[15]   European Cooperation for Space Standardization. *ECSS-Q-ST-70-12C*. http://ecss.nl/standard/ecss-q-st-70-12c-design-rules-for-printed-circuit-boards-14-july-2014/.

[16]   honeywell. *SET/RESET FUNCTION FOR MAGNETIC SENSORS*. https://aerospace.honeywell.com/en/~/media/aerospace/files/application-note/an213_set_reset_function_of_magnetic_sensors.pdf. Application Note: Set/Reset Function of Magnetic Sensors: AN-213.

[17]   William S. Levine. *The Control Handbook. Volume 1*. 352000/7e41e674f3a128dc4db24da4ae845f24. URL: 352000/7e41e674f3a128dc4db24da4ae845f24.